NISTIR 4422

METROLOGY FOR SPACE POWER: METROLOGY DEVELOPMENT AND SURVEY OF SPACE-BASED MEASUREMENTS

G. J. FitzPatrick
J. K. Olthoff
E. D. Simmon
C. P. Fenimore, Jr.

U.S. DEPARTMENT OF COMMERCE
National Institute of Standards
and Technology
Center for Electronics and
Electrical Engineering
Electricity Division
Gaithersburg, MD 20899

Prepared for:
Strategic Defense Initiative Office
Survivability, Lethality, and
Key Technologies Program

Sponsored by:
Defense Nuclear Agency under
Project SG SA/Space Power and
Power Conditioning, Work Unit 00071

September 1990

U.S. DEPARTMENT OF COMMERCE
Robert A. Mosbacher, Secretary
NATIONAL INSTITUTE OF STANDARDS
AND TECHNOLOGY
John W. Lyons, Director

Foreword

Portions of this work are an accumulation of information provided by individuals from other agencies. The authors wish to acknowledge the following individuals whose contributions were essential to the preparation of this report.

D. Allred (Defense Nuclear Agency)
W. Bangs (NASA, Goddard Space Flight Center)
B. Banks (NASA, Lewis Research Center)
K. Chan (JPL California Institute of Technology)
G. Cotty (Martin Marietta)
G. Coultas (NASA, Johnson Space Center)
D. Dalton (NASA, Goddard Space Flight Center)
G. Day (NIST, Electromagnetic Technology Division)
N. Divine (JPL, California Institute of Technology)
W. Elsen (NASA, Goddard Space Flight Center)
W. Fawcett (JPL, California Institute of Technology)
H. Garret (JPL, California Institute of Technology)
R. Kichak (NASA, Goddard Space Flight Center)
W. Kolarik (Texas Technological University)
H. Marderness (JPL, California Institute of Technology)
J. McElwee (NASA, Space Station Station Freedom)
H. Moffitt (NASA, Johnson Space Center)
M. Pongratz (Los Alamos National Laboratory)
M. F. Rose (Space Power Institute, Auburn University)
P. Schrantz (COMSAT)
B. Siegel (NASA, Office of Space Sciences and Applications)
J. Smith (NASA, Lewis Research Center)
J. Stovall (ORNL)
W. Taylor (NASA, Marshall Space Flight Center)
L. Travis (NASA, Goddard Institute for Space Studies)
J. Zimmerman (NASA, Marshall Space Flight Center)

This report summarizes the progress of three technical investigations conducted during CY 89. Although reasonable efforts have been made to ensure the reliability of the data presented, it must be emphasized that this is an interim progress report and that further experimentation, analysis, and research may be performed before the conclusions from any of these investigations are formally published. It is therefore possible that some of the observations presented in this report will be modified, expanded, or clarified by our subsequent research.

Table of Contents

List of Figures

List of Tables

METROLOGY FOR SPACE POWER: METROLOGY DEVELOPMENT AND SURVEY OF SPACE-BASED MEASUREMENTS

G. J. FitzPatrick, J. K. Olthoff, E. D. Simmon,
and C. P. Fenimore, Jr.

Abstract

This report documents the technical progress in the three investigations which make up the project "SDI Measurement Techniques" funded by the Strategic Defense Initiative Office and performed by the Electricity Division of the National Institute of Standards and Technology. The first investigation develops part of the mathematical background needed for assessing the reliability and efficiency of the diagnostics used in the development of pulsed power components and systems. The signature of measurement failure is demonstrated in an electro-optic system. The detection of such failures is the first stage in remotely restoring the integrity of a measurement system. The detection of measurement nonlinearities is critical in assuring reliability of diagnostic equipment. Through comparative measurements, characteristic signatures of nonlinearities in an electro-optic voltage measurement system have been detected. The errors are of the order of 1% in magnitude. Nonlinearities in a conventional detector system have been investigated through appropriate models. These studies are the first step in an effort to improve reliability of diagnostics in remote applications through error identification, detection, and correction. The second investigation assesses the applicability of magneto-optic sensors for measuring microsecond and submicrosecond current pulses. The results of comparative measurements of fiber optic current sensors with conventional detectors is reported here. The optical sensing systems have sufficient bandwidth for measurement of submicrosecond-risetime pulses but sensor stability is a problem, especially in remote applications. The third investigation involves the accumulation of existing information necessary to support an effective measurement development program. The results of an in-depth study of existing space-based measurement techniques are reported, and the findings from these results indicate that present space-based measurement systems are inadequate for anticipated SDI requirements.

1 INTRODUCTION

The goals of the investigations in the SDI Measurement Techniques project are to identify metrology needs of various SDI programs and to improve the reliability of diagnostic measurement systems in remote applications. In the first phase of the program, a survey of the present and anticipated metrology needs of several SDI space power programs was conducted. The survey resulted in a report covering the present state of the art of ground-based diagnostic sensors and also cataloged the improvements in sensitivity and accuracy of diagnostics required by the SDI [1]. This report continues this activity with an investigation of diagnostics with space flight experience, i.e., measurement systems that have already been used in space applications.

The present work also includes development of the mathematical background necessary for ensuring reliability of remote diagnostic systems and investigations of optical current sensors. Measurement reliability is critical in remote applications. To ensure measurement reliability, parallel sensors based on different measurement technologies (and thereby having different nonlinear error characteristics) can be used to determine measurement errors in one or the other of the sensors. This requires identification of the error sources and knowledge of the characteristics of the measurement errors and sensitivity to be able to detect small nonlinearities. The work presented here is a first step in an effort to develop techniques for error detection and correction in remote diagnostic systems: nonlinearities of the order of 1% in measurements using an electro-optic voltage measurement system have been detected. System models have also been used to test the technique with nonlinearities in conventional voltage measurement systems. These characteristic error signatures illustrate the usefulness of the technique in detecting measurement errors with parallel sensors.

Fiber optic current sensors provide distinct advantages over conventional current sensors for space applications: in particular, they are smaller and lighter, and have greater immunity from electromagnetic interference (EMI). Thus, they are attractive for use in space. They are now being used in ground-based developmental pulsed power systems. The results of an investigation into their applicability to measurements of pulsed currents is reported here. They have the bandwidth necessary to measure submicrosecond-risetime pulses accurately, but their stability is dependent on environmental effects and improvements are needed before they can be reliably used in space.

This report begins with the measurement reliability investigation. The magneto-optic current-sensor test results are presented in the following chapter and the report concludes with the continuation of the space power metrology survey.

2 MEASUREMENT RELIABILITY: THE DETECTION OF NONLINEARITIES

2.1 Introduction

The reliability of a measurement is assured when a high level of confidence is attached to the measurement with its estimated error. Confidence is usually established in a practical measurement system by multiple comparisons with a system in which reliability is assured. Conversely, a measurement system fails when there is a loss of confidence in its results. Catastrophic failure, in which there is a total loss of a reportable measurable result, is neither the most likely nor the most troublesome mode of failure. A sensor which delivers a signal which is obviously in error, can be ignored. A sensor which fails but continues to report a measurement represents an undetected failure; it destroys the integrity of the information and impairs control.

Is it possible to detect a single failure in a measurement system by a comparison process? In the case studied here, it is possible to detect certain classes of measurement failures. The system under study employs two sensors which are complementary in the sense that they employ converting devices based upon different technologies to measure a single quantity. These sensors are a Kerr-cell and a voltage divider. When the system is in-calibration the individual sensors respond to their inputs according to the system model. The failure of a single sensor means that one component of a complementary system responds nonlinearly to its input.

The recalibration of a measurement system in which a component part has failed is the ultimate goal of measurement reliability. This goal can be decomposed into two parts. The first of these is the detection of measurement failures; the second is system identification and, if possible, measurement correction. In this report we present a tool for detection: signature analysis of measurement failure. The system studied measures a transient voltage pulse by using a resistive voltage divider and a Kerr electro-optic technique. Before correction is possible the nature of the failure must be found. The fact of failure may be established when the measurement data no longer fit the system model. A single numerical measure may establish that failure has occurred. However, additional information is contained in the time-resolved data. The lack-of-fit by the data to the system model provides a characteristic signature which we display in the case of three types of nonlinearities(i.e., measurement failures):

- A time base shift between the two waveforms.
- A quadratic nonlinearity in the photodetector for the Kerr-effect measurement.
- An overdriven photodetector.

Each of these is detectable, by which is meant that analysis of the two signals produces a characteristic signature for each nonlinearity which warns of failure. This is the first step of a process. With sufficiently detailed information about the failure mechanisms of the components of the system, it may also be possible to identify the failure and to apply corrections [2]. We demonstrate how time-base shifts are identified and corrections are applied to data in the present NIST test measurement system.

The next section of our paper compares and contrasts the present approach to that of Adibi [3]. We also consider its relation to other measurement and reliability problems. The third section is a presentation of the Kerr measurement system. It is followed by a discussion of the mathematical basis for the comparison of the divider with the Kerr-cell measurements. Finally, the characteristic signatures for three failure modes are shown. A proof that detectability and identifiability are not equivalent precedes the summary.

2.2 Background

The reliability of complex systems depends on the performance of individual components. Thus, information on component reliability provides vital input to models of the system. In the area of component reliability, Kolarik and co-investigators [4, 5] have demonstrated the use of various computational tools with potential application to pulsed-power life testing. These tools are primarily intended for use at the design and development stages.

These tools include techniques for factor analysis and hypothesis testing [4] for analyzing test data of individual components. In addition, the enhancement of systems reliability through use of redundant components has been considered in [5]. The analytical tools of that work are derived from readily available proprietary software packages. These techniques may provide prior estimates for reliability and may be of value in designing sufficient redundancy to assure reliable performance.

The reliable performance of measurement systems depends on assuring the accuracy of measurements. The work of Adibi and Thorne [3] addresses some of the aspects of remotely calibrating complex measurement systems found in commercial power systems. The measurements are linearly related and the computational techniques produce an estimate of the corrections which must be applied to reconcile the disparate measurements. The computation provides a detection scheme for identifying out-of-calibration instruments. The nonlinearity of the present system and the use of electro-optic elements is a distinctive feature of the present work.

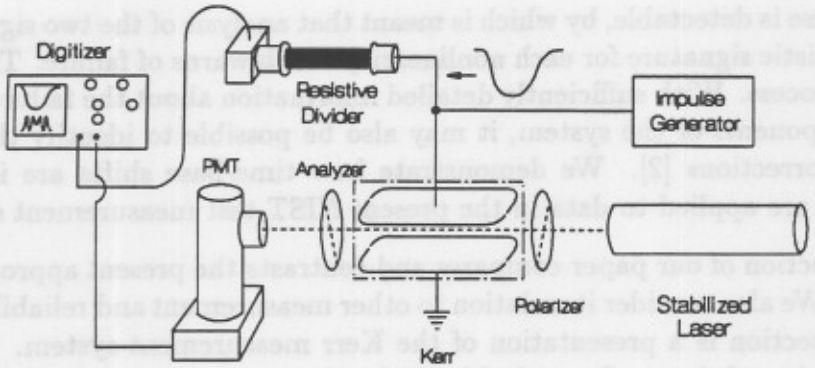

Figure 1. The experimental configuration for Kerr-cell vs. resistive divider comparison.

2.3 Experimental Setup

The experimental configuration used for this study is shown in Figure 1. The impulse generator is a pulse-forming network consisting of discrete inductors and capacitors that produces an output pulse having a 4-μs risetime. The Kerr cell is constructed of a polytetrafluoroethylene (PTFE) body with stainless steel plate electrodes and filled with purified nitrobenzene. It is connected in parallel with the precision resistive voltage divider to the output of the impulse generator. A stabilized helium-neon laser is used with a side-window photomultiplier tube (PMT) detector. The intensity variations that are measured by the PMT result from the change of the state of polarization of the incident light beam induced by the Kerr liquid when the voltage is applied to the plates. As used here, the PMT has a highly nonlinear output for a dc supply voltage of 800 V, but the output is linear over a limited range of light intensities for a supply voltage of 360 V [6]. The outputs of the resistive divider and PMT are measured with an 8-bit, dual channel, digitizing oscilloscope having a 100 MHz bandwidth.

The resistive divider has a low-inductance wirewound high-voltage arm made by counterwinding identical lengths of a very low temperature coefficient resistive wire upon a cylindrical ceramic substrate. The low-voltage arm is a discrete resistor that gives an overall divider ratio of 5000:1. The divider is immersed in insulating oil to eliminate corona and to minimize the physical size required to withstand the full voltage (and consequently minimize its response time). The response time of this precision divider to a step voltage having a risetime of a few nanoseconds is less than 10 ns. The two waveforms which are acquired have the form as seen in Figure 2. The number of fringes in the Kerr cell photo-intensity is ideally related to the voltage by the nonlinear Kerr law. Measurement failure, as described in the next section, is caused by the nonlinear response of either the voltage divider or of the photomultiplier tube to its input.

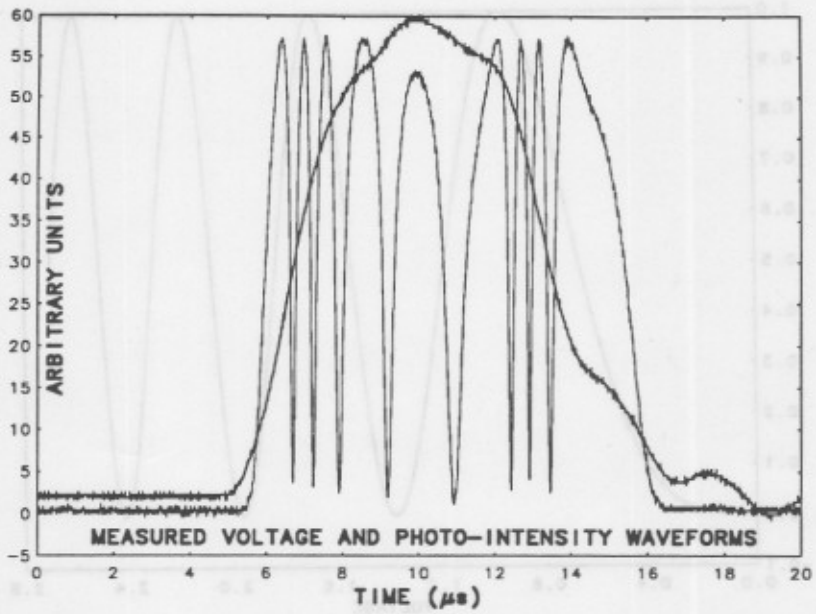

Figure 2. The traces of the voltage and Kerr optical waveforms are displayed simultaneously for an overdriven detector. The general fringe pattern is entirely characteristic of Kerr-cell measurements. The applied voltage waveform has a single maximum.

2.4 The System and its Nonlinearities

The detection of nonlinearities is based on a numerical fitting of the coefficients in a model for the measurement system. The use of modern analytical techniques and the application of curve-fitting software to digital data allows for detectibility of nonlinearities at a level close to that of the intrinsic noise. The model for our system is based on the Kerr electro-optic effect. This effect produces a linear birefringence effect proportional to the square of the electric field. The result is modulation of the intensity of a beam at the output of the crossed polarizer system shown in Figure 1. In an ideal measurement system the path is fixed and the optical intensity, L, is related to the voltage applied across the optical cell, U, by :

$$L(t) = L_m \sin^2 \left\{ \frac{\pi}{2} \left(\frac{U(t)}{U_m} \right)^2 \right\}. \tag{1}$$

L_m is the maximum light intensity passed by the Kerr system and U_m is the Kerr cell constant which is determined by the Kerr coefficient and the cell geometry. The measured optical intensity, I, may differ from the actual intensity, L, due to a variety of measurement errors, including nonlinearities. The signatures of two examples of such nonlinearities are given. These are a quadratic nonlinearity in the photodetector,

$$I(t) = \alpha L + \beta L^2, \tag{2}$$

and an overdriven detector operating outside its linear regime.

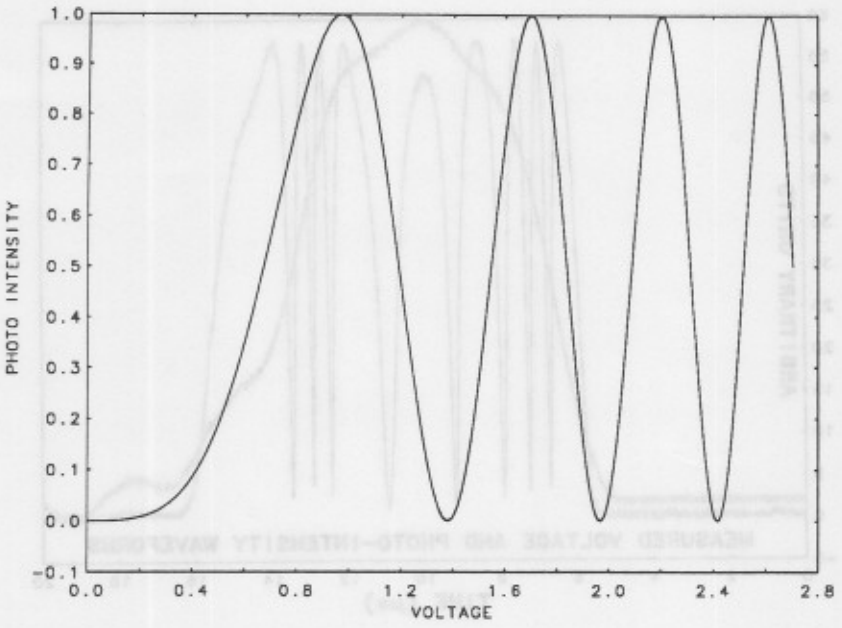

Figure 3. The ideal Kerr-law voltage-intensity (U *vs.* L) relationship with a voltage peak chosen to generate 7.5 fringes. Time is absent from this plot and from the fitting procedure. The fitting minimizes the total residual between the measured voltage-intensity data and the U *vs.* L 'curve'.

In the absence of any errors, the Kerr Law implies that at every instant the values of photo-intensity and of voltage will lie on the curve shown in Fig. 3 in the state space consisting of pairs (V, I). When the errors are due to a change in the gain of either the divider or the photodetection system, identification of error sources is possible with the software developed for this project. The coefficients, U_m and L_m which appear in the Kerr Law, may be determined from the data as a part of the nonlinear least squares fitting procedure. This requires the minimization of the sum-of-squares lack-of-fit for the discrete data expressed by:

$$R^2 = \sum_{t_i} \left[L_m \sin^2 \left\{ \frac{\pi}{2} \left(\frac{V_i}{U_m} \right)^2 \right\} - I_i \right]^2 . \tag{3}$$

The minimum is not unique; however, in many cases the desired values of U_m and L_m may be found as perturbations of the calibrated values. The fitting is based on the Levenberg-Marquardt algorithm for nonlinear optimization and employs the software, SUMSL[1], found in the public-domain Core Mathematical Library (CMLIB)[1] [7]. A simple technique for identifying a time delay betwen V and I is presented in the next section.

[1]The citation in this document of any publicly-available software in no way constitutes an endorsement by NIST nor does it imply that the software is the best available for the application.

2.5 Signature of Measurement Failure

The signature of a nonlinearity in the detection system is found as the point-by-point lack-of-fit $I_i - L(V_i)$ as a function of L. In Figure 4(a) the result of this comparison is shown for a numerically-generated 0.25% quadratic nonlinearity in the photodetector. For values of $\alpha = 0.99$ and $\beta = 0.01$ in Equation 2, the maximum effect occurs at $L = \frac{L_m}{2}$. In the absence of noise, the signature of the failure is readily seen to be quadratic. Each branch of the residual plot corresponds to one fringe of the Kerr intensity plot. In Figure 4(b) the results for experimentally introduced nonlinearity are shown. In this case the detector is overdriven at a voltage for which the nonlinearity is to be expected [6]. The noise of the system is not estimated independently. However, this characteristic pattern is seen for a range of over-voltages on the photodetector.

In each case, the signature for an in-calibration system is a straight line with a noise level appropriate to the measurement system. The effect of noise on this detection heuristic is such that the nonlinearity can be observed when it is comparable with the noise. The large number of points permits averaging which effectively increases the signal-to-noise ratio.

In the case of a time delay between $V(t)$ and $I(t)$ for a pulse waveform the nonlinearity has the form

$$I(t) = L(t + \Delta t). \tag{4}$$

For a pulse with $\Delta t > 0$, the signature of the time-origin shift as seen in the state space of (V, I) pairs is a left-shifted curve where V is increasing and a right-shifted curve where V is decreasing. For either positive or negative Δt, the data traverse a hysteresis loop about the ideal (V, I) curve as in Figure 5.

In the case of a digitized pulse measurement, the identification of the delay may be achieved by a fast and simple alternative to the full nonlinear fitting as in (3). The technique does not require that U_m and L_m be known. In the absence of a time delay, the points (V_i, I_i) should lie on a single curve as in Figure 3 for both rising and falling values of V_i. Using this principle, one finds the channel shift s, which brings the shifted data points (V_{i-s}, I_i) closest together on the rising and falling portions of the (V, I) curve. Specifically, for each value of the shift, s, the voltage data V_{i-s} are grouped into a number of discrete levels V_b (bins) with $b = 1 \ldots B$, and the scatter of the I_i is summed within each bin. The total scatter, S, is given by

$$S(s) = \sum_{b=1}^{B} \sum_{i, V_{i-s} \simeq V_b} \sigma^2(I_i). \tag{5}$$

The time delay is that value of s which minimizes the scatter. Using this technique it is possible to find delays of as little as one or two sampling intervals without difficulty even when the number of fringes is small.

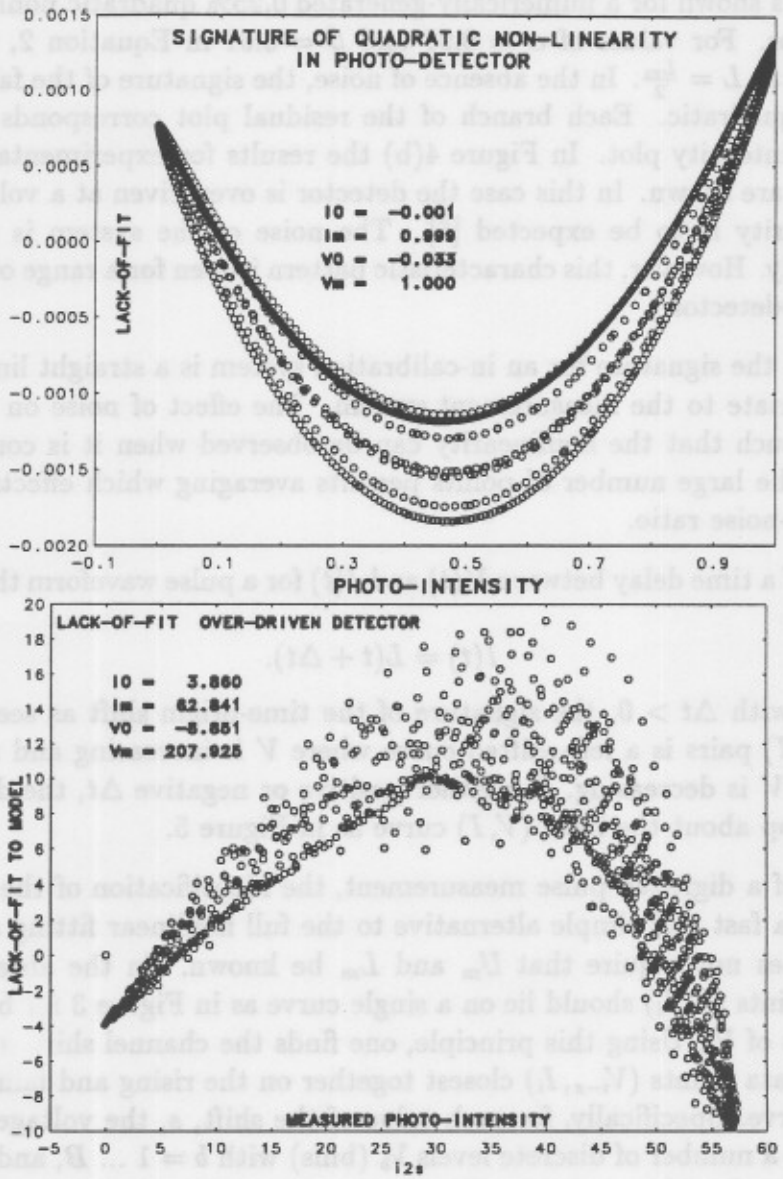

Figure 4. The signatures of nonlinearities arising from: (a) a simulated quadratic nonlinearity of 0.25% in the photo-detector, (b) and an overdriven photodetector - experimental data.

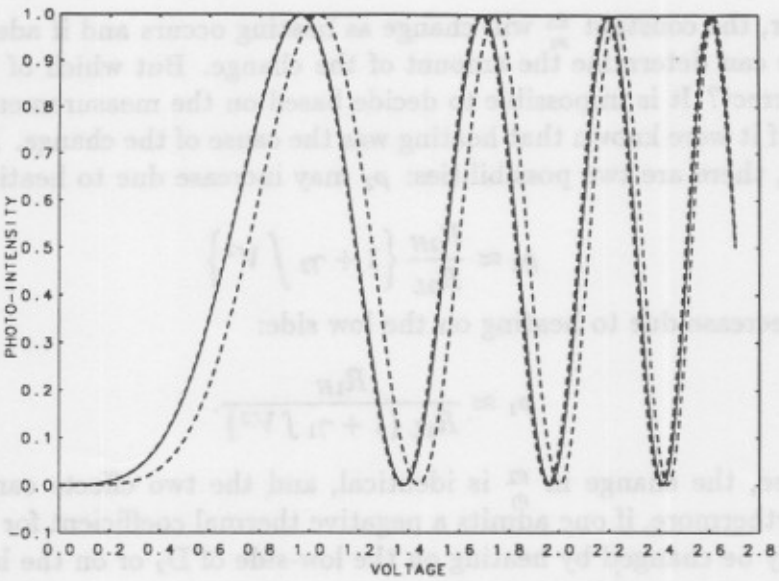

Figure 5. A time-delayed voltage waveform produces the leading (V, I) trajectory. Delay compensation is chosen to minimize hysteresis.

2.6 Detectability Not Equal To Identifiability

A simple example of measurement comparisons demonstrates that in redundant measurement systems detectability is not equal to identifiability and suggests the power of complementarity in such comparisons. As an example of a redundant measurement system consider two voltage dividers, D_1 and D_2, each with its ratio, ρ_1 and ρ_2. That is to say, for any voltage waveform, $V(t)$, the measured voltages are v_1 and v_2, where $V(t) = \rho_1 v_1(t)$ and $V(t) = \rho_2 v_2(t)$, respectively. The model for our measurement system relates the two measurements by:

$$v_1(t) = \frac{\rho_2}{\rho_1} v_2(t). \tag{6}$$

A change in one of these two parameters ρ can be detected but not identified. Even worse, common nonlinear failures may not be identifiable. To demonstrate the ambiguity in a simple comparison measurement, note that the ratio, ρ, is related to the resistances R_H, on the high side and R_L on the low side of the divider by $\rho = \frac{R_H}{R_L} + 1 \approx \frac{R_H}{R_L}$. One simple form of nonlinearity in the measurement system is the Joule heating of a resistor. Neglecting heat losses the resistance takes the form:

$$R(t) = R_o \left\{ 1 + \gamma \int_o^t V^2(s) ds \right\}. \tag{7}$$

If the heating coefficient, γ, is large for one resistor component and negligible for the others, then one of the ratios, ρ_1 or ρ_2, will change and the system will be detectibly out-of-calibration because the system constant $\frac{\rho_2}{\rho_1}$ will have changed. Failure is detected.

In particular, the constant $\frac{\rho_2}{\rho_1}$ will change as heating occurs and if adequate data are available we can determine the amount of the change. But which of the dividers, if either, is correct? It is impossible to decide based on the measurements of v_1 and v_2 alone, even if it were known that heating was the cause of the change. If, for example, $\frac{\rho_2}{\rho_1}$ increases, there are two possibilities: ρ_2 may increase due to heating on the high side

$$\rho_2 \approx \frac{R_{2H}}{R_{2L}} \left\{ 1 + \gamma_2 \int V^2 \right\} \tag{8}$$

or ρ_1 may decrease due to heating on the low side:

$$\rho_1 \approx \frac{R_{1H}}{R_{1L} \{ 1 + \gamma_1 \int V^2 \}}. \tag{9}$$

In either case, the change in $\frac{\rho_2}{\rho_1}$ is identical, and the two effects cannot be distinguished. Furthermore, if one admits a negative thermal coefficient for the resistance, the ratio may be changed by heating on the low-side of D_2 or on the high side of D_1, so that any component of this simple system could be the source of the failure. This renders identification for this out-of-calibration system ambiguous and its correction impossible.

By contrast, the highly nonlinear system model (1) makes a change in the gain of either the divider or the photodetector both detectible and identifiable. A change in U_m amounts to a change in the (single) wavelength of the sinusoid in the system model and cannot be confounded with a change in its amplitude, L_m. Furthermore, the fitting procedure outlined in 2.4 allows one to compute the changed values. In the spirit of the detection scheme, each class of nonlinearity which is to be identified must be separately examined to determine if its effects may be ambiguous. The present work does not address ambiguity and identification of nonlinear failure.

2.7 Summary

The long-term reliability of space-based power measurement systems depends on both the reliability of the components and on the ability to detect failure and, if possible, to recalibrate defective components remotely. The task of maintaining and restoring measurement reliability has been analyzed here as a dual problem of failure detection and of system identification and correction. The detection and identification of measurement failure due to a change in gain or to a time-delay has been demonstrated in a measurement system based on the comparison of sensors which have nonlinearly related outputs. By comparing a voltage divider with a Kerr electro-optic cell it is possible to avoid ambiguity regarding the source of a measurement failure. It is in this sense that the comparison is referred to as complementary, rather than redundant. For certain nonlinearities in the sensor characteristics it is possible to detect failure but, with the exception of the time-delay, the identification and correction is not considered here. For the most part, these results are intended as a demonstration

of the feasibility of failure detection. The immediate challenge in developing these techniques is to catalogue the various failure mechanisms in the component sensors of complex systems and to expand the identification and correction methodology to include additional types of nonlinearities.

3 MAGNETO-OPTIC CURRENT SENSORS

3.1 Introduction

Deployment of electrical power systems in space requires that the systems be highly reliable and have as small a volume and weight as possible. The same is true of the sensors used to monitor system operation [8]. Conventional high-voltage and current sensors tend to be bulky, but in the past decade compact and lightweight optical sensors have come into use [9, 10, 11]. Optical sensors have also been used to support calibrations performed at NIST [12]. These sensors are constructed of materials whose optical properties are influenced by the presence of externally-applied electric or magnetic fields. Although field-sensitive, they can be used to measure currents and voltages through the use of appropriate design geometries. In addition to being smaller and lighter than conventional detectors, they offer the important advantage of having greater immunity to electrical interference and thus operate more reliably and accurately in electrically "noisy" environments. Optical sensors are also coming into use in the electric power industry. Magneto-optic sensors are now being developed for current metering on power lines [13]. The assessment of optical current sensors to the measurements of submicrosecond pulses performed in the present work may also have spinoff applications such as in the testing of power apparatus.

It is very desirable to be able to use these sensors in the space environment for the advantages they offer: small size, light weight, and electrical isolation. But the harsh conditions and remote operation required of this relatively new sensor technology in space also poses questions concerning how their long-term measurement accuracy can be assured. The purpose of the task reported here is to evaluate the applicability of magneto-optic current sensors to the measurement of microsecond and submicrosecond impulses. This work is a preliminary step in an effort to identify and develop methods for correction of optical sensor measurement errors for remote operation, such as in the unfriendly environment of space.

One way to assure measurement accuracy is through the use of redundant sensing by comparison of the outputs of two or more detectors that measure the same quantity in parallel. The detectors may be identical, but preferably they should be based upon different technologies to make it improbable that they would "fail" in the same manner and conceal measurement errors. The error sources must be identifiable so that it can be known when one of the devices is providing inaccurate data and by how much it is in error. This comparative measurement approach has been used in the present study. Simultaneous measurements of the submicrosecond-risetime currents have been made with a well-characterized conventional detector and an optical current sensor in parallel. The comparison of the outputs of the two detectors demonstrate the magneto-optic sensor measurement errors, its limits of applicability, and where improvements in the technology are required. Transient impulse currents are

more difficult to measure accurately than steady-state ac or dc currents because they require wide-bandwidth instrumentation. Measurement errors are much more significant with optical sensors for low-amplitude peak currents ($< 10^3$ A) than for larger ones due to the inherently low sensitivity of the Faraday magneto-optic effect. Most sensors have been developed for measurement of currents greater than 10 kA [14]. Measurements of current pulses having risetimes of a few hundred nanoseconds and peak amplitudes of less than 200 A have been made in this work in order to assess measurement errors.

This section of the report begins with a description of the design and operation of optical current sensors, including the different types of sensing elements and measurement system configurations. A presentation of the results of the comparison measurements and discussion of the sources of measurement errors then follows. The section concludes with a summary of the work and discussion of where improvements in the technology are needed to ensure reliability in remote applications.

3.2 Design and Operation of Magneto-Optic Current Sensors

Optical current sensors utilize the Faraday magneto-optic effect that in the presence of a magnetic field results in a rotation of the plane of polarization of linearly polarized light. For current sensing, the glass sensing element is usually designed to surround the current-carrying conductor so that, according to Ampere's circuital law, the rotation of the polarization is proportional to the current passing through the sensor. Two types of elements are used: bulk elements, such as flint or Schott glass, and silica fiber elements which offer potentially greater sensitivity. The rotation of the beam can be measured with an analyzer at the sensor output and a single photodetector. In principle, greater sensitivity is achieved at low current levels by using two photodetectors to measure orthogonal components of the polarization of the beam at the sensor output. The operation and design of the optical sensors are now described.

3.2.1 Principles of Operation

The Faraday effect in optical materials such as silica enables the use of polarimetric detection systems to measure magnetic fields within the optical sensor. This first-order effect relates a rotation in the plane of polarization of linearly polarized light to the magnetic field as follows:

$$\theta = \int_L V\vec{B} \cdot d\vec{l} \tag{10}$$

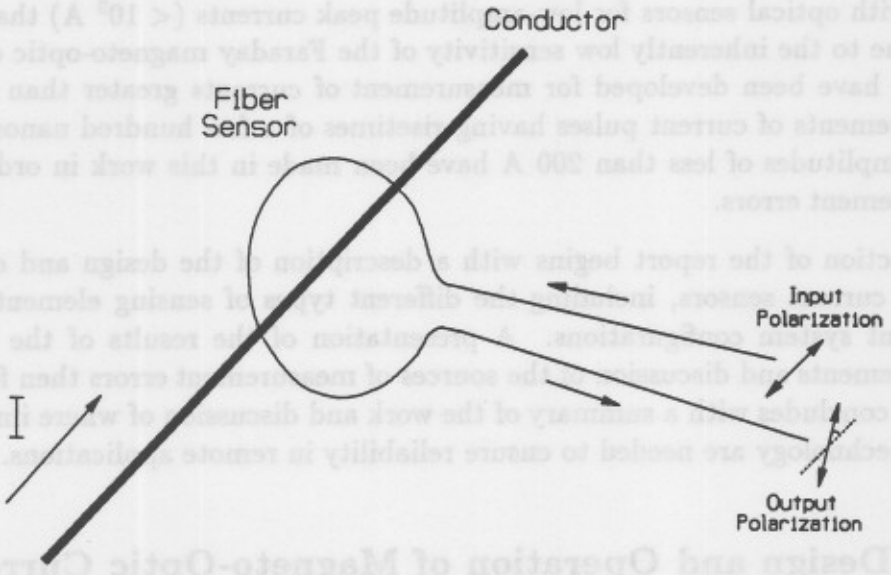

Figure 6. Optical current sensing element.

where V is a material parameter known as the Verdet constant, $\vec{B}$ is the magnetic flux density, and the integration is made along the optical path. For current measurements, the geometry of the sensing element is chosen to form a loop that encircles the current. Ampere's circuital law can then be utilized to relate the induced rotation of the beam to the current I passing through the sensing element:

$$\theta = \mu V \oint \vec{H} \cdot d\vec{l} \tag{11}$$

$$= \mu V N I \tag{12}$$

where N is the number of turns in the fiber sensor and the constitutive relationship, $\vec{B} = \mu\vec{H}$, has been used. A single-loop fiber sensing element is shown in Figure 6. The plane of polarization of the input beam is rotated by an angle proportional to the current. This rotation appears as a change in the measured intensity at the photodetector after the output beam from the sensing coil passes through an analyzer. The relationship between the measured intensity and beam rotation θ when the transmission axis of the output polarizer is oriented at 90° to the unperturbed beam is :

$$I = I_o sin^2(\theta) \tag{13}$$

where I_o is the maximum intensity of the beam (i.e., the intensity measured at the output when the plane of polarization is aligned with the transmission axis of the analyzer). The sensitivity of the sensor can be improved by taking the beam at the sensor output and splitting it into two orthogonal components oriented at angles of $\pm\pi/4$ to the plane of the unperturbed linearly polarized light and measuring the intensity with two photodetectors. These intensities are given by:

$$I_1 = I_o sin^2(\theta + \pi/4) \tag{14}$$

$$I_2 = I_o sin^2(\theta - \pi/4) \tag{15}$$

Taking the difference of the outputs of the two detectors yields a response function that is a function of 2θ and dividing the difference by the sum of the outputs eliminates the dependence of the response function on the peak intensity, I_o:

$$R = (I_1 - I_2)/(I_1 + I_2) \tag{16}$$

$$= sin(2\theta) \tag{17}$$

Substituting Equation 12 into 17:

$$R(I) = sin(2\mu VNI) \tag{18}$$

The response function R(I) for the ideal dual photodetector system is shown in Figure 7. The response function of Equation 18 calculated from the output of the two detectors has greater sensitivity to small currents than that for a single detector (Equation 13), as well as having the advantage of being independent of the input beam intensity, I_o. The optical system configurations are described in the next section.

3.2.2 Measuring System Configurations

A typical dual-detector measurement system configuration is shown in Figure 8. The output of the laser is coupled by a microscope objective into an optical fiber which transmits the beam to the sensing element. A second fiber carries the beam from the sensing element to the detectors. At the output of the second fiber, the beam is divided by a polarizing beam splitter (Wollaston prism) into its two orthogonal components. Through appropriate orientation of the half-wave plate at the fiber output, the response function of Equation 18 can be utilized with the measured intensities of the orthogonal components of the output beam for improved sensitivity over single photodetector configurations.

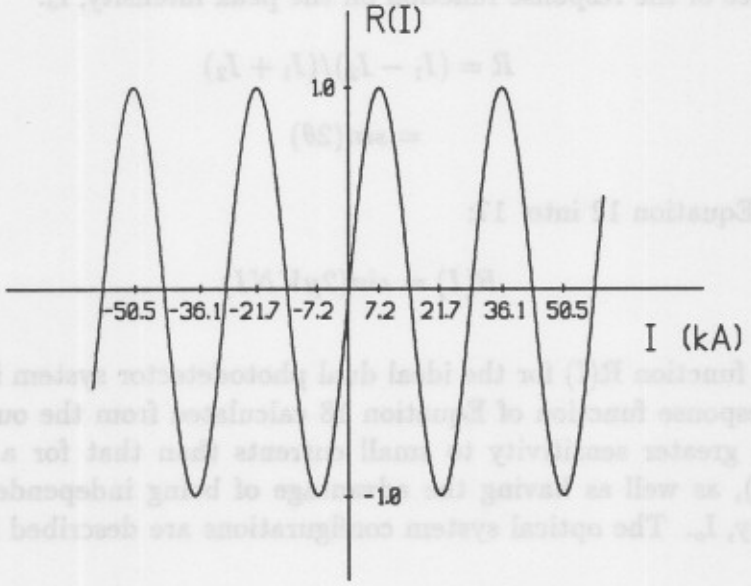

Figure 7. Response function for the dual photodetector configuration.

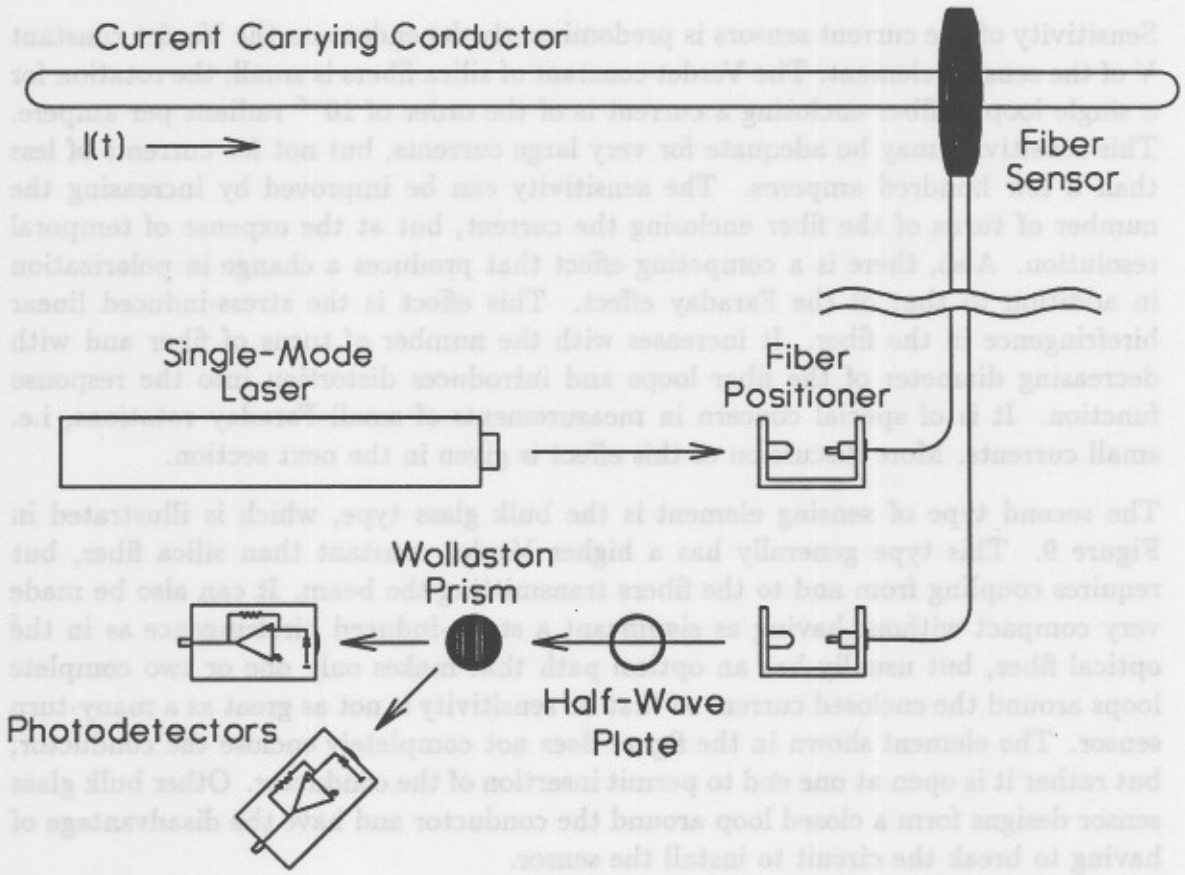

Figure 8. Magneto-optic current sensor system. The basic measurement system consists of a light source, fiber optics, optical sensing element, polarimetric optics, and photodetectors.

The sensing element is composed of a section of optical fiber that exhibits the Faraday effect, that is, a rotation of the plane of polarization of linearly polarized light passing through it in proportion to the magnetic flux density, according to Equation 10. Two types of sensing elements are used in magneto-optic sensors: optical fiber elements and bulk glass elements. Typical elements are Schott glass, flint glass, and silica glass fibers. The most convenient implementation is the optical fiber element where a section of optical fiber, which may either be a section of the fiber used to transmit the beam or a separate piece, is used as the sensing element. This is done by winding the fiber into a loop around the current-carrying conductor, as illustrated in Figure 8.

Sensitivity of the current sensors is predominantly dependent on the Verdet constant V of the sensing element. The Verdet constant of silica fibers is small; the rotation for a single loop of fiber enclosing a current is of the order of 10^{-6} radians per ampere. This sensitivity may be adequate for very large currents, but not for currents of less than a few hundred amperes. The sensitivity can be improved by increasing the number of turns of the fiber enclosing the current, but at the expense of temporal resolution. Also, there is a competing effect that produces a change in polarization in addition to that of the Faraday effect. This effect is the stress-induced linear birefringence in the fiber. It increases with the number of turns of fiber and with decreasing diameter of the fiber loops and introduces distortion into the response function. It is of special concern in measurements of small Faraday rotations, i.e. small currents. More discussion of this effect is given in the next section.

The second type of sensing element is the bulk glass type, which is illustrated in Figure 9. This type generally has a higher Verdet constant than silica fiber, but requires coupling from and to the fibers transmitting the beam. It can also be made very compact without having as significant a stress-induced birefringence as in the optical fiber, but usually has an optical path that makes only one or two complete loops around the enclosed current so that its sensitivity is not as great as a many-turn sensor. The element shown in the figure does not completely enclose the conductor, but rather it is open at one end to permit insertion of the conductor. Other bulk glass sensor designs form a closed loop around the conductor and have the disadvantage of having to break the circuit to install the sensor.

3.3 Measurement Errors

Since the sensors used in this study were of the fiber-optic and not the bulk-glass type, the measurement errors discussed here relate primarily to optical fibers. The errors in the measurements can be categorized by their source: the optical fiber, the light source, and the detectors. Additionally, there are measurements errors in the

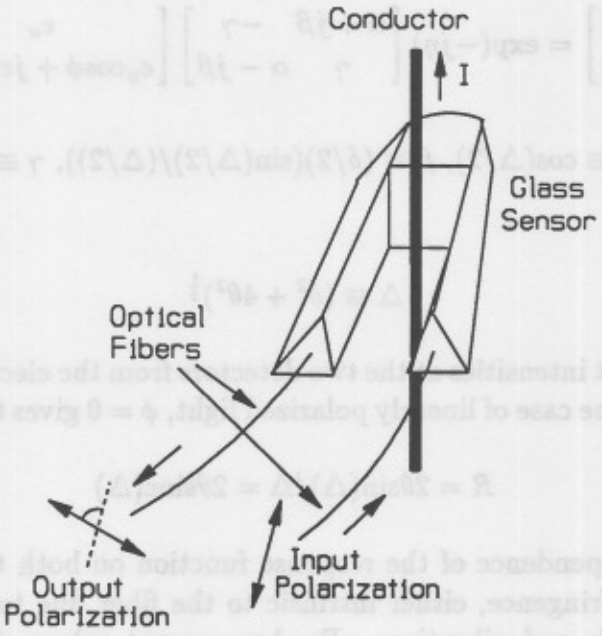

Figure 9. Bulk glass sensing element. The loop is open on one end to permit insertion of the conductor.

oscilloscope or digitizer used to measure the detectors' output, but typically the other errors dominate.

The optical fiber itself produces a change in the polarization of the light traversing it through its intrinsic birefringent properties: anisotropies in the indices of refraction in the fiber core are introduced during the manufacturing process, produced by bending and twisting of the fibers, or caused by direct pressure on the fiber. The change in polarization produced by these birefringences tend to obscure the Faraday rotation, especially for low currents. Rogers has analyzed the relation of the light at the input and output of a fiber to include both linear birefringence δ and Faraday rotation θ. The effects are incorporated in a matrix relating the electric field components of the light at the input of the fiber to those emerging from it [15]:

$$: \begin{bmatrix} E'_x \\ E'_y \end{bmatrix} = \exp(-j\eta) \begin{bmatrix} \alpha + j\beta & -\gamma \\ \gamma & \alpha - j\beta \end{bmatrix} \begin{bmatrix} e_x \\ e_y \cos\phi + j e_y \sin\phi \end{bmatrix} \tag{19}$$

where j $\equiv \sqrt{-1}$, $\alpha \equiv \cos(\Delta/2)$, $\beta \equiv (\delta/2)(\sin(\Delta/2)/(\Delta/2))$, $\gamma \equiv \theta(\sin(\Delta/2)/(\Delta/2))$, and

$$\Delta \equiv (\delta^2 + 4\theta^2)^{\frac{1}{2}} \tag{20}$$

Calculating the light intensities at the two detectors from the electric field components of Equation 19 for the case of linearly polarized light, $\phi = 0$ gives the response function R:

$$R = 2\theta \sin(\Delta)/\Delta = 2\theta \,\mathrm{sinc}(\Delta) \tag{21}$$

which shows the dependence of the response function on both the Faraday rotation and the linear birefringence, either intrinsic to the fiber due to its construction, or introduced by bends and vibrations. For low current values, the induced Faraday rotation is small and if the linear birefringence is significant ($\delta \gg 2\theta$), the response is:

$$R \approx 2\theta \sin(\delta)/\delta = 2\theta \,\mathrm{sinc}(\delta) \tag{22}$$

Since the linear birefringence is sensitive to vibrations and is not constant in general, it is necessary to minimize it relative to the Faraday rotation. In the optimal case, the induced rotation dominates and the linear birefringence, induced or intrinsic, is negligible ($\delta^2 \ll (2\theta)^2$). The response function when the linear birefringence is negligible is:

$$R \approx \sin(2\theta) \tag{23}$$

The condition $\delta^2 \ll (2\theta)^2$ is met for current sensors measuring large currents or by deliberately introducing additional circular birefringence by twisting the fiber [16]. This produces a bias in the output curve of the sensor that has the effect of moving

the quiescent operating point (when no current passes through the sensing element) away from the region where the linear birefringence is most influential (i.e., where Equation 22 holds).

A major contributor of errors in the measurement of small currents is transient stress-induced birefringence in the optical fiber sensors. This stress arises from vibrations in the fiber and distorts the output response function as described by Equation 22. Precautions must be taken to minimize vibrations by encasing the sensor and connecting optical fibers in a rigid case or vibration-damping media.

The light source used with a single detector configuration must be stable since any variation in the output is assumed to be due to the magnetically-induced change in polarization of the light. Many laser and laser diode light sources, including the helium-neon source used in this work, have intensity variations of 0.1% or less. Stabilized laser sources have even smaller variations in intensity and long-term drift. Changes in the source intensity are, in principle, not so critical when the dual detector configuration is used because the theoretical response function given by Equation 18 is independent of the light source intensity, I_o.

The photodetectors are required to have a wide bandwidth in order to be capable of measuring fast transients, and must also be linear over the range of intensities to be measured. In the dual detector configuration, the photodetectors are required to be matched as closely as possible in gain and bandwidth. The detectors' characteristics are temperature-dependent. Temperature compensation must be used if the sensors are used in an environment with large temperature variation [16].

An optical current sensor utilizing the dual detector configuration with an optical fiber sensing element was used in parallel with a conventional detector to measure impulse currents having submicrosecond risetimes. These results are discussed in the next section.

3.4 Comparisons with Conventional Sensors

In order to evaluate the response of a sensor to an input pulse, the input pulse must be known. This can be accomplished through the use of either a very stable generator having known output or a well-characterized sensor used in parallel with the one to be evaluated so that they are measuring the same quantity at the same point in the circuit. The latter approach was taken here and was implemented using a wide-bandwidth voltage probe inserted into a 50Ω coaxial test line at the same point as the magneto-optic current sensor. The outputs of the sensors were compared from simultaneous measurements of the pulses in the line. The tests illustrate the deficiencies of the optical current sensor as it is presently configured: high detector noise level, relatively low sensitivity, instability of the light source, and stress-induced birefringences in the optical fibers. The tests also showed that the optical current sensor had

sufficient bandwidth and that submicrosecond-risetime pulses in the range of tens of amperes were measurable. The tests indicated where modifications in the measurement system were needed: improvements in the optical components, light source, and detectors will provide better sensitivity and reduced measurement uncertainties. The test procedures, configuration, and results are described in detail in the following sections.

3.4.1 Circuit Configuration

The circuit configuration used for the simultaneous measurements is shown in Figure 10. The Marx-type pulse generator produced pulses having risetimes of 200 ns and falltimes of 60 μs to half of the peak value. The pulses were launched into the coaxial test line via a section of 50 Ω coaxial cable and transition section shown in the figure. The coaxial transmission line containing the sensors provided a system where the current and voltage were directly related through the 50Ω characteristic impedance of the line. Thus the relationship between the current to be measured by the optical sensor I_{os} and the voltage to be measured by the resistive probe V_{rp} are related through:

$$V_{rp} = I_{os} Z_c \tag{24}$$

where Z_c is the characteristic impedance of the coaxial line of 50 Ω. The voltage probe and optical current sensor are located at the same point in the coaxial line. The coaxial test line is terminated in its characteristic impedance to avoid reflections

.

The high voltage probe consisted of a noninductive wirewound 10k Ω resistive divider, rated for dc voltages of up to 10 kV. The response time of the probe was a few nanoseconds. From probe design considerations, it is believed that the probe did not introduce significant loading of the test circuit. This was confirmed when no detectable differences in the measured currents were observed regardless of whether the probe was present in the circuit or not.

The magneto-optic sensor was of the all-fiber type described in section 3.2.2 used with a 2 milliwatt helium-neon laser source having 632.8 nm wavelength. The output of the laser was sufficiently linearly polarized to use it without a polarizing element. The source was focused into a single-mode fiber with a 20X microscope objective having a focal length of 0.8 mm. The fiber system comprised three components: two light-transmitting fibers and the coiled fiber sensor. The first optical fiber transmitted the light to the sensing element where they were joined with a fiber connector. The beam traversed the sensor and was transmitted into a second single-mode fiber of the same type as the first through a similar connector.

The sensing element also consisted of a length of single-mode optical fiber, provided by Gordon Day of NIST's Electromagnetic Technology Division in Boulder, Colorado.

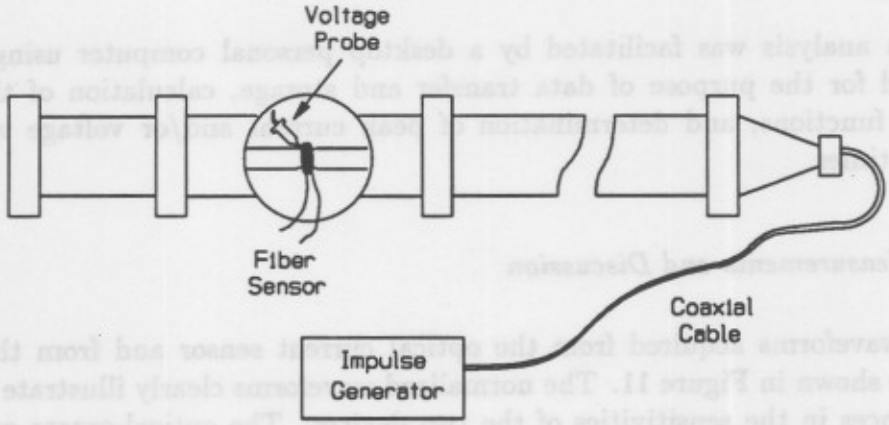

Figure 10. Test circuit configuration. The Marx-type impulse generator launches the fast-risetime pulses into the 50 Ω coaxial line. The current and voltage sensors measure the pulse at the same point in the line.

The element was a 4.4 cm diameter multiturn coil. Because winding such a coil of relatively small diameter introduces significant bend-induced birefringence, the fiber had been annealed to relieve the birefringence [17]. The output of the second single mode fiber was focused on a Wollaston prism which split the beam into its two orthogonal polarization components, whose intensities were measured using two photodetectors. The detectors were wide-bandwidth photodiode/opamp pairs used in a transimpedance configuration with a single 50 kΩ feedback resistor. The 3 dB bandwidth was approximately 10 MHz.

The output of the detectors was measured using a dual-channel digitizer having a 10-bit (0.1%) amplitude resolution and maximum sampling rate of 100 megasamples per second. The effective 3 dB bandwidth of 100 MHz was adequate to measure the pulses accurately. The output of the high-voltage probe was monitored by a scan converter having an effective bandwidth of 1 GHz and 9-bit (0.2%) amplitude resolution.

The data analysis was facilitated by a desktop personal computer using software developed for the purpose of data transfer and storage, calculation of the optical response functions, and determination of peak current and/or voltage values and response times.

3.4.2 Measurements and Discussion

Typical waveforms acquired from the optical current sensor and from the voltage probe are shown in Figure 11. The normalized waveforms clearly illustrate the effect of differences in the sensitivities of the two devices. The optical-sensor output has significant noise due to the relatively small changes in optical intensity being measured. To reduce the effect of the considerable noise in the current-sensor output, the peak values were calculated by finding the difference between the average of thirty digitized points at the peak (about 300 ns) and the baseline which was taken as the average of thirty points prior to the rise of the pulse. The pulses used in this work had risetimes of about 200 ns followed by a much slower exponential decay, falling to half the value of the peak in a time of about 60 ns. The peak output of the voltage probe was similarly found by averaging the digitized data over the time ranges corresponding to those used for determining the current-sensor peak outputs.

For the currents measured in this study, the theoretical dependence of the response function on current is approximately linear, as shown in Figure 12(a). The deviation from linearity over this current range is less than 0.1%, as demonstrated in Figure 12(b), which is a graph of the difference between sin(2NVI) and its argument 2NVI.

A major limitation of optical fibers used as sensors is birefringence produced by bending when forming the coil. An estimate of the theoretical bending birefringence

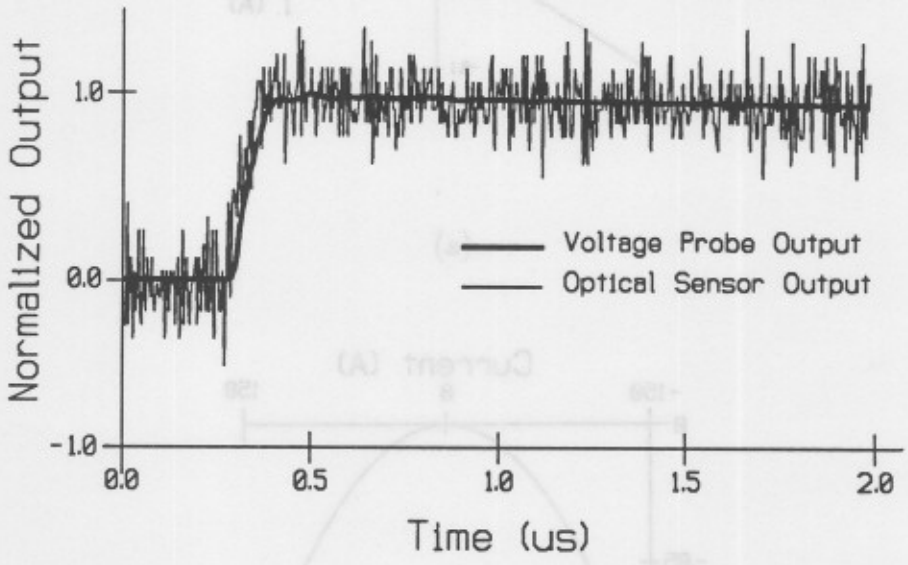

Figure 11. Normalized outputs of optical current sensor and voltage sensor

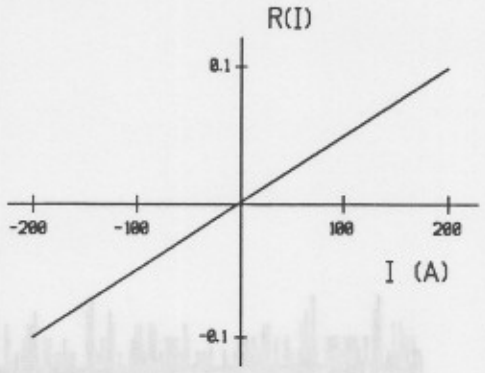

(a)

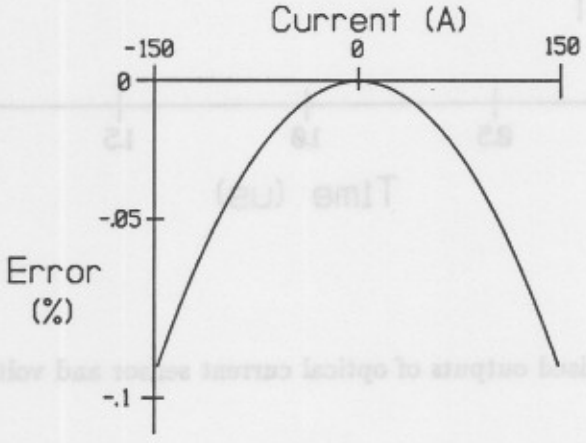

(b)

Figure 12. Theoretical dependence of peak output of current sensor on peak current. (a) Response function, R(I), over linear region. (b) Deviation from linearity (see text).

of the coil before annealing is given by [18]:

$$\delta_B = (0.85/\lambda)(r/R)^2 \tag{25}$$

From this equation, the calculated bending birefringence is $\delta_B = 10.8$ radians/m for a fiber diameter of 2r = 125 μm, a coil diameter of 2R = 4.4 cm, and the wavelength of 633 nm. The total path length in the coil is:

$$L = 2N\pi r \tag{26}$$

which is 6.5 m for N = 47 turns of this sensor. The total linear birefringence is then:

$$\delta = \delta_B \times L \tag{27}$$

or 70.2 radians. For the currents measured in this study, this intrinsic birefringence would dominate, and the magneto-optic effect, that is polarization changes due to the current in the conductor, would not be detectable making the sensor useless. However, because the sensor is annealed, the bending birefringence is greatly reduced, and small currents are measurable, as will now be shown from actual measurments.

The comparison of peak currents calculated from the measured voltage peaks and the peak output from the current sensor is shown in Table 1. The response function of the sensor was checked over a range from 3.7×10^{-3} to 7.7×10^{-3} corresponding to peak currents between 58 and 122 A. The dependence of the current-sensor output on the peak current using the values of Table 1 is shown in the graph of Figure 13 to be approximately linear. A slope of 6.15×10^{-5} A^{-1} with an intercept of -2.3×10^{-5} for zero current, was found by a linear regression analysis of the measured data. Ideally, the sensor output should be zero when the current is zero, but the extrapolation to a nonzero value is attributed to uncertainties in the measured data.

The slope for the fitted curve can be compared with the theoretical response function to determine the residual linear birefringence in the sensor. When linear birefringence dominates the Faraday rotation, the output is:

$$R \approx 2NVI\text{sinc}(\delta) \tag{28}$$

This response is linearly proportional to the current, assuming that the linear birefringence of the fiber is constant, which is a reasonable assumption on the time scale of the pulse. In the ideal case of no linear birefringence ($\delta = 0$), the theoretical output given in Equation 22 is also linearly proportional to the current for small Faraday rotations:

$$R \approx 2NVI \tag{29}$$

Table 1. Comparison of voltage probe output and optical sensor output response function R(I). Current is calculated from the voltage probe output. The data represent the average of three measurements.

I (A)	R(I) ($x10^{-3}$)
58	3.7
76	4.7
91(*)	5.2(*)
104	6.3
122	7.7
(*)Average of two measurements.	

where the approximation of $\sin(2NVI) \approx 2NVI$ has been used for small currents. The difference between the ideal case of Equation 29 and the linear birefringence-dominated case of Equation 28 is that the response for the latter is much smaller. When linear birefringence dominates, the small-signal output is scaled by a factor of $\text{sinc}(\delta)$, which is always smaller than unity.

The linear birefringence, δ, can be found from the slope of the line of Figure 13. From Equation 28, this slope should be equal to $2NV\text{sinc}(\delta)$. Using the value of the Verdet constant for the fiber at 633 nm wavelength of 4.63×10^{-6} radians/ampere-turn, and N = 47 turns, $\text{sinc}(\delta)$ is found to be 0.141 from the slope of the fitted curve, which corresponds to a total linear birefringence of $\delta = 2.7$ radians. The output for this sensor is reduced to 14.1% of the output for the ideal case when there is no linear birefringence present. The maximum induced rotation in these measurements of 0.053 radians for a peak current of 122 A is much smaller than the birefringence of 2.7 radians, justifying the use of the linear birefringence-dominated approximation (Equation 28). Although for the currents in this range (58–122 A) the linear birefringence effect is much larger than the induced rotation, this effect is considerably reduced from the initial birefringence before the coil was annealed. The response of the sensor before annealing found from Equation 27 using $\delta =$ 70.2 radians, is only 1.3% that of the ideal (zero linear birefringence) case given by Equation 29, and would be undetectable due to the small current amplitude. Annealing the fiber sensor reduced the intrinsic linear birefringence by 96% to 2.7 radians. Although the response is only about 14% of the ideal small-signal response, it is still measurable.

The pulse risetime found from the current sensor data for peak currents ranging from 74 to 131 A was 189 ns. This value compared well with the risetime of 196 ns calculated from the voltage sensor data. Without improvement in the signal-to-noise

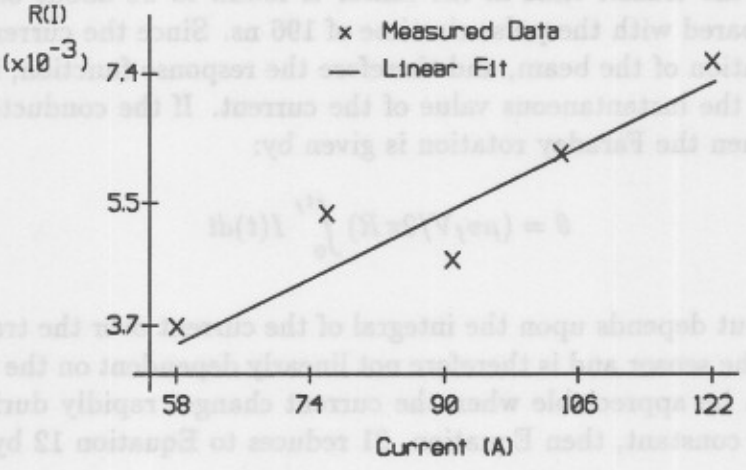

Figure 13. Measured dependence of the response function, R(I), on peak current. The solid line is a linear fit to the measured peak values.

ratio, the measurement uncertainties in the current sensor data are still too large to provide accurate evaluations of the pulse parameters.

In addition to measurement noise, another concern about the accuracy of the data is nonlinearities introduced in the measurement when the current changes significantly during the time it takes the light beam to travel through the sensor. Application of Ampere's circuital law (Equations 11 and 12) assumes that the magnetic field intensity is constant as the light traverses the path enclosing the conductor. The transit time of the beam within the sensor is simply the physical path length, L, divided by the velocity of the beam, v_f. The path length of this sensor is 6.5 m, the velocity is found from the speed of light, c, and the refractive index, n, of the fiber:

$$v_f = c/n \tag{30}$$

Using n = 1.5, the transit time in the sensor is found to be about 33 ns, which is significant compared with the pulse risetime of 196 ns. Since the current is changing rapidly, the rotation of the beam, and therefore the response function, is not linearly proportional to the instantaneous value of the current. If the conductor is centered in the sensor, then the Faraday rotation is given by:

$$\theta = (\mu v_f V/2\pi R) \int_0^{t_f} I(t)dt \tag{31}$$

The sensor output depends upon the integral of the current over the transit time, t_f, of the beam in the sensor and is therefore not linearly dependent on the current. This nonlinearity can be appreciable when the current changes rapidly during this time. If the current is constant, then Equation 31 reduces to Equation 12 by substituting Equation 30.

Because the sensor transit time is large in comparison with the risetime of the current pulse used in the measurements made in this study, the optical-sensor output is not linearly proportional to the current during the rising edge of the pulse where the current changes most rapidly. Once the current pulse reaches the peak, however, it decays much more slowly and does not reach its half-value until about 60 μs. The peak values of the optical current sensor output given in Table 1 were calculated by averaging over thirty data points after the peak (about 300 ns) because the current is essentially constant over this range of the pulse. These peak values are directly proportional to the instantaneous current.

3.5 Summary

The magneto-optic current sensor used in the present study is typical of the fiber-optic type used in dc, ac, and pulsed-current measurements. The sensor has been tested by

comparison with another wide-andwidth sensor for measurement of submicrosecond-risetime currents with peak amplitudes in the hundred ampere range. The sensor has been shown to have sufficient bandwidth, but stability of the sensor in the present configuration is inadequate for impulse-current measurements of high accuracy.

Changes in the configuration will yield improvements in the sensitivity of the optical fiber sensor. A light source having higher power and less intensity variation could be used to improve the signal-to-noise ratio of the photodetector. Although the response function for the dual detector configuration is independent of the source intensity, I_o, the response of the individual photodetectors (Equation 13) is not. Use of a larger source intensity will produce a greater change in the photodetector output than that of the present configuration for the same current. The result is improvement in signal-to-noise ratio.

Other improvements could be achieved with further reduction in the residual birefringence in the coiled fiber sensor. If the residual birefringence could be reduced, then the slope of the response-function/current curve (Figure 13) could be increased, with resultant improvement in sensitivity.

Future work will focus on incorporating these changes for an improvement in device sensitivity. Nonlinearities in the magneto-optic current sensor measurements will be investigated through further comparison measurements with stable, wide-bandwidth conventional current detectors. These nonlinearities will be determined in a similar fashion to that described in the previous chapter which described investigation of a Kerr electro-optic measurement system through comparison with conventional voltage sensors. The sources of the measurement nonlinearities will be identified through their characteristic signatures. The long-range goal of the work is to enable correction of nonlinearities in remote measurement systems.

4 SURVEY OF SPACE-BASED MEASUREMENTS

4.1 Introduction

Development of complex, high-power, long-mission space platforms for SDI applications will require extensive use of state-of-the-art instrumentation and control devices. These devices will be essential to validate the performance of the overall system and therefore must be reliable, long-lived, automated, remote, autonomous and reconfigurable. Of primary concern is the interaction of the diagnostic device with the space environment. Any sensor designed for space-based SDI applications must withstand long-term exposure to the harsh space environment encountered in low-earth orbit. This requires a resistance to debris impact, temperature variations, radiation damage, atomic-oxygen corrosion, charging due to the ionosphere, high-g launch forces, and long-term vacuum and micro-gravity exposure.

A previous study [1] reported on the capability of present state-of-the-art ground-based measurement systems to meet the anticipated metrology requirements of SDI power systems. While existing ground-based instrumentation may be adequate for most ground-based developmental and operational testing, certain problem areas clearly exist where the extrapolation of these techniques to space deployment will be extremely difficult or perhaps impossible. It is therefore useful to investigate the types of measurements and the types of instrumentation which are presently being used to monitor and control various types of spacecraft. Thus, a program was initiated to obtain a general overview of the types and magnitude of parameters presently measured in space, and the types of hardware required to perform these measurements.

The next four subsections report the information obtained in this study. The first section (4.2) reports on the measurements made on existing spacecraft (the space shuttle, satellites, the Voyager space probes, and various sounding rocket experiments), while the next section (4.3) deals with anticipated measurements which will be required on several future space projects, including the space station. Section 4.4 then discusses the methods by which components and systems are presently tested and approved for space use and summarizes some of the on-going experiments dealing with the interaction of components with the space environment. Section 4.5 summarizes the findings of the study and draws some conclusions with regard to the implications of these findings to the SDI.

It should be noted that this study emphasizes engineering or "housekeeping" types of measurements, i.e., measurements which are necessary for the operation of the spacecraft. This report does not include any discussions of the metrology techniques used for navigation or orientation of spacecraft. Nor are measurements used for space

science experiments discussed in great detail. Each of these systems has unique measurement capabilities, many of which may equal or exceed the capabilities discussed here.

4.2 Present Space-Based Measurement Systems

4.2.1 Space Shuttle

Of all currently-operational space hardware, the space shuttle is perhaps the most complex and fully instrumented. Practically every type of parameter which would be expected to be monitored on an SDI platform is measured on the space shuttle. In some cases, the magnitude of the measured variables begins to approach the extreme values anticipated for nuclear-powered weapon platforms.

Temperature measurements made on the space shuttle are very diverse. Cryogenic temperatures (−250 °C) are measured to monitor the status of liquid hydrogen and oxygen in the fuel tanks. Type K thermocouples are used for these measurements with approximately 1–2% uncertainty.

More moderate temperatures are measured throughout the structure of the shuttle. Many thermistors are used to monitor the temperature of the shuttle body beneath the heat tiles. During re-entry the temperatures approach 350 °F. Temperatures are also measured inside the payload bay (and elsewhere on the shuttle structure) to indicate temperature differentials. If during orbit a large temperature differential is allowed to form, the structure of the shuttle will flex due to thermal expansion and contraction. Too large of a temperature differential will produce sufficient structural flex such that the payload doors will be unable to open or close. Other moderate temperature measurements are made to monitor the crew's cabin temperature and also to control the heaters which prevent freeze-up of the propulsion system and other liquid feed lines on the shuttle.

Higher temperatures are measured in several locations on the shuttle. The skin temperature (on the outside of the heat tiles) is monitored during reentry, with temperatures approaching 2000 °F. The temperatures of the hot gas regions of main shuttle engines are continuously measured using several redundant platinum resistance thermometers with ~1% uncertainties. Temperatures average approximately 1450 °F with a maximum allowable temperature of 2200 °F. The output from these sensors (4 sensors per engine) is analyzed by the main engine controllers to determine if overheating is occurring and if a shut-down is necessitated. Higher temperatures (3000–4000 °F) were measured inside the solid rocket boosters during the first 5 space shuttle flights. The sensors were tungsten/rhenium thermocouples which were obviously used for only a single measurement.

Pressure measurements are also common and very diverse on the space shuttle. The

highest pressures approach 7500 psi and are found in the high-pressure systems of the main shuttle engines. These pressures are measured with bonded strain gauges on metal diaphragms which are protected from the high temperatures of the engines and provide measurements with 1–3% uncertainty with a frequency response of about 300 Hz. Elsewhere in the fuel lines, pressures are measured using piezosensors with greater frequency responses so as to be able to monitor higher frequency (~4 kHz) pressure fluctuations due to vortex shedding at high flow rates. High pressures (4000–6000 psi) are also measured in the high-pressure helium tanks aboard the shuttle. Low-magnitude differential pressures (1–2 psi) are measured between various compartments inside the shuttle structure to ensure that atmosphere is allowed to escape from these volumes during ascent.

Total cabin pressure is continually measured with 5% uncertainty, while partial pressure measurements of O_2 are made to ensure that oxygen levels do not increase above 30%. Any higher levels of oxygen represent a fire hazard inside the crew compartment. Other pressure measurements include monitoring the air pressure on the exterior of the shuttle wings during lift-off. These measurements are made to determine the amount of lift provided by the shuttle wings during ascent. Lift by the wings of the shuttle during take-off is unnecessary (the thrust provided by the solid rocket boosters is sufficient) and could possibly cause structural damage. The measurements are made by hundreds of transducer pressure gauges which are reused on each launch and appear to survive the space environment quite well. The tire pressure is determined indirectly by measuring the strain on the inside wheel rims. The current method will soon be replaced by a miniature pressure transducer placed inside the valve stem of the tire.

Because of the large amount of liquids required for the operation of the shuttle, volume determinations are an important class of measurements. Many of these measurements are made more difficult by the lack of gravity and because of the cryogenic nature of the liquids. Volume measurements in the external fuel tank are simplified and are easily made using platinum wire heat-transfer level sensors because they are only made while on the ground or during acceleration. On the orbiter, where microgravity conditions exist, several methods are employed to determine volume. For some tanks, capacitance level meters are used, but measurements can only be made during acceleration. For the propellant tanks, the liquid is displaced by helium from a high-pressure gas reservoir. The decrease in overall helium pressure as the gas expands to replace the liquid is an indication of the loss of propellant. This method obviously assumes that there are no leaks in the helium system. For some cryogenic liquids, a capacitance probe measures the density of the homogeneous liquid inside the tank thereby determining the mass of the remaining liquid in the tank. In coolant loops, which are designed to be closed systems, a reservoir whose volume is determined by a piston, contains any extra liquid not presently circulating in the loops. A decrease in the volume of the reservoir (after adjustments for changes in temperature and pressure) indicates the presence of a leak. Lastly, the amount of water onboard

the shuttle is determined by the displacement of a bellows. Water is created in the fuel cells at a rate greater than can be used by the crew, so periodic dumping is required when the reservoir becomes too full.

Flow measurements onboard the shuttle are generally made by either measuring a differential pressure across an orifice or by turbine-type flow meters. In some cases, sensors are used to measure the rotational speed of the turbopumps thus providing an indication of flow rates. Presently the highest flow rates (which exist in the main engines) are determined solely by calculation. However, research is being done on a technique to determine very high flow rates using the monitoring of vortex shedding.

Electrical measurements on the space shuttle are fairly straightforward since the magnitudes are quite moderate and extremely high precision is not required. The distribution system of the shuttle is 120 VAC (400 Hz) and the primary service bus is 28 VDC. Voltages are measured using standard A-D converters while currents are monitored using viewing resistors or LC circuits.

Many other operational variables are monitored during a space shuttle mission. Accelerometers measure vibration of the turbopumps supplying H_2 and O_2 to the main engines. Smoke detectors (ionization-chamber type) monitor for the presence of smoke in the cabin and in the avionics air cooling system. Crew radiation exposure is determined by film badge detectors, but real-time radiation monitoring is no longer done. Position sensors (microswitches) indicate the open/closed status of various doors and hatches, and other microswitches determine when the wheels touch the ground during landing so that different flight control systems can be initiated.

It should be noted that while the types of measurements and metrology systems used on the space shuttle are similar in nature to those required by various SDI systems, the shuttle hardware is used for short-term, manned missions. This presents a vastly different set of measurement requirements than those expected for the long-term (10 years), unmanned missions anticipated for SDI platforms. In general, the measurement systems employed on the space shuttle are similar to generic systems presently used in the aerospace industry. Little work has been done to extend the use of these sensors to long-term space use.

4.2.2 Satellites

Unlike the space shuttle, satellite missions are usually long-term (2–10 years) and unmanned, thereby more closely resembling SDI types of missions. However, the magnitude of the measured housekeeping variables on an average satellite are many orders of magnitude less than those anticipated on SDI platforms, and the required measurement uncertainties on satellites are not particularly stringent. For example, bus voltages on satellites are routinely set at 28 VDC and measured with 8-bit ac-

curacy. However, components on a satellite will normally operate on any voltage between 23 and 32 VDC, thus making

high-accuracy voltage measurements unnecessary in most cases.

While an "average" satellite may monitor more than 100 parameters, most of the measurements are very similar in nature. Some examples of typical measurements are: Battery charging current (~10A) is routinely monitored to assess the status of solar cells and battery systems. Temperatures are measured throughout the satellites with ±1°C uncertainty over ranges of about −60°C to +60°C at a rate of one sample per second. The rotation rate of the stabilizing gyros (2–5 rotations/min) is monitored along with the attitude of the satellite with respect to the sun or the earth. Pressures are monitored by various transducers in the propellant systems and near the exhaust nozzles. Lastly, status signals ("heartbeats") are monitored by a central control unit to assess which subsystems are presently in operation.

Overall, the information obtained from flying hundreds of satellites for the past three decades forms an invaluable data base for SDI programs to draw from, particularly in regard to low-magnitude measurements and system reliability (see section 4.4.2). However, the experience gained from satellite development does little toward advancing the metrology capabilities necessitated by the most extreme requirements of the SDI program.

4.2.3 Voyager Space Probes

The mission objectives of the Voyager space probes are to conduct exploratory investigations of the Jupiter and Saturn planetary systems and of the interplanetary medium [20]. Both spacecraft were launched in 1977 and have remained operational (in most respects) for the past 13 years. Thus the Voyager probes represent two of the longest continually operating spacecraft on record. Information concerning the long-term performance of the sensors and diagnostics on the probes is useful in the design of long-mission space platforms.

Like the satellites discussed in the previous section, the measurements required by the housekeeping systems are reasonably routine. Voltages measurements range from 30 VDC to 50 VAC, while temperature measurements range from –90°C to 240°C. The scientific apparatus on the Voyager missions possess more demanding metrology requirements than the engineering support systems. These experiments are listed in Table 2 but the details are presented elsewhere [20, 21] and will not be discussed here.

In order to remain functional for its entire mission, the Voyager subsystems were designed with high reliability components and extensive redundancy. This philosophy has worked extremely well as is evident by the continuing operation of the spacecraft. As of late 1989, only two out of 75 temperature sensors on Voyager I have failed. Of course some system failures have occurred. Voyager I is presently using its backup

Table 2. Scientific investigations on the Voyager mission

Experiment	Primary Experiment Objectives
Imaging Science	Imaging of planets and satellites at resolutions and phase angles not possible from earth. Atmospheric dynamics and surface structure
Infrared Radiation	Energy balance of planets. Atmospheric composition and temperature fields. Composition and physical characteristics of satellite surfaces and Saturn rings.
Photopolarimetry	Methane, ammonia, molecular hydrogen, and aerosols in atmospheres. Composition and physical characteristics of satellite surfaces and Saturn rings.
Ultraviolet Spectroscopy	Atmospheric composition including the hydrogen to helium ratio. Thermal structure of upper atmospheres. Hydrogen and helium in interplanetary and interstellar space.
Radio Science	Physical properties of atmospheres and ionospheres, planet and satellite masses, densities, and gravity fields. Structure of Saturn rings.
Cosmic Ray Particles	Energy spectra and isotopic composition of cosmic ray particles and trapped planetary energetic particles.
Low Energy Charged Particles	Energy spectra and isotropic composition of low energy charged particles in planetary magnetospheres and interplanetary space.
Magnetic Fields	Planetary and interplanetary fields
Planetary Radio Astronomy	Planetary radio emissions and plasma resonances in planetary magnetospheres.
Plasma Particles	Energy spectra of solar-wind electrons and ions, low-energy charged particles in planetary environments, and ionized interstellar hydrogen
Plasma Waves	Electron densities and local plasma wave-charged particle interactions in planetary magnetospheres.

Table 3. Charged particle and nuclear radiation design requirements for Voyager

Particles	Peak Flux ($cm^{-2}s^{-1}$) Shielded	Fluence (cm^{-2}) Shielded	Peak Flux ($cm^{-2}s^{-1}$) Unshielded	Fluence (cm^{-2}) Unshielded
Protons*	9×10^7 (E > 1 MeV)	5×10^{12} (20 MeV Eq)	9×10^7 (E > 1 MeV)	5×10^{12} (20 MeV Eq)
Electrons	2×10^8 (E > 0.4 MeV)	4×10^{12} (3 MeV Eq)	2×10^8 (E > 0.4 MeV)	4×10^{12} (3 MeV Eq)
RTG** Neutrons ($1.0 \leq E \leq 3.0$ MeV)	80	1×10^{10}	10	1×10^9
RTG** Gamma ($0.3 \leq E \leq 3.0$ MeV)	3200	1×10^{3}*** Rad(Si)	350***	100*** Rad(Si)

NOTE:
*Proton flux and fluence assume a 1 MeV cutoff. Proton levels for true external surface problems are higher than those above. The level is 3.1×10^8Rad(Si).
**Radioiosotope Thermal Generator (RTG)
***Unshielded ionization dose level is really controlled by electron and proton environments above.

Flight Data Subsystem, has a partially disabled tracker, and has several semiconductor memory anomalies. Almost all of the scientific instruments on Voyager I are experiencing some operational deficiencies, and two are completely non-operational. Despite these failures, Voyager has continued to be sufficiently functional to perform its required tasks. However, in many cases, it was earth-based reprogramming or improved data analysis which allowed the experiments to be performed when a hardware failure occurred.

Of equal interest to the SDI is the performance of the Voyager probes during and after their exposure to the Jupiter and Saturn radiation environments. Based on previous measurements of the Jupiter radiation belts, appropriate radiation hardening, parts selection, circuit design evaluation, and shielding actions were taken to strengthen the Voyager resistance to radiation effects. Despite these precautions, Voyager I experienced at least 42 anomalies resulting in power-on resets while in the inner Jovian magnetosphere [22]. These anomalies are thought to be caused by internal charging of components due to high energy (E≥40 keV) electrons in the magnetosphere. The radiation design requirements for the Voyager missions are summarized in Table 3 [20].

Table 4. SPEAR-I instruments

Two spherical current collectors and graded booms
HV power supply and capacitors
Transient current and voltage measurement
Steady-state current and voltage measurement
TV imaging of current collector sheath
Photometer detection of specific emission lines in current collector sheath
Hollow cathode plasma contactor
Ambient neutral pressure at vehicle
Ambient plasma density/temperature (Langmuir probe)
Ion and electron detectors
VLF and HF wave detectors
3-axis magnetometer

4.2.4 SPEAR I

The Space Power Experiments Aboard Rockets (SPEAR) program was initiated by the SDI organization to investigate the interaction of high-voltage pulsed power systems with the low earth-orbit space environment. SPEAR-I, which was flown in December, 1987, consisted primarily of instruments sufficient to measure the currents and voltages associated with applications of high voltages stored on capacitors connected to two spheres exposed to the space environment. [24] The entire experiment was flown on a sounding rocket capable of reaching an apogee exceeding 300 km, with an experimental time of approximately 400 s. The basic purpose of the mission was to measure the interaction of the high voltage with the plasma sheath surrounding the spacecraft, and to determine the suitability of the space environment as an insulating medium for high-voltage applications. The use of space as an insulator is considered essential by many for the successful deployment of SDI systems requiring high voltage such as free electron lasers and neutral particle beams.

The instrumentation which was included in the experiment is listed in Table 4. While the results of the entire experiment [24] are of interest, we discuss here only the performance of some selected measurement systems employed during the investigation.

High-voltage (up to 45 kV) measurements (both steady-state and transient) were made using a 1000:1 frequency compensated voltage divider. Steady state current measurements (up to 2 amperes) were made using a 2.2 Ω viewing resistor while transient current signals were measured using Rogowski coils. These measurements represent the first attempt to measure high-magnitude electrical signals in space. The sensors operated as designed, however, the measurement devices were all contained in a sulfur hexafluoride filled chamber and were not exposed to the space environment. The fact that no breakdown was observed between the two charged spheres exposed to the space environment is encouraging for the possibilities of using vacuum as a high-voltage insulator on spacecraft. However, the short duration of the experiment

and the high ambient pressures observed (see below) indicate that some questions concerning the suitability of the space environment for use as an insulator for high voltage systems have yet to be answered.

The ambient neutral pressure surrounding the rocket was measured by a cold cathode ionization gauge with a range of 10^{-3} to 10^{-7} torr and a time resolution of 1 ms. During the experiment, pressures were seen to vary only between 10^{-3} and 10^{-5} torr, several orders of magnitude above anticipated values, thus suggesting considerable outgassing from the rocket during the elapsed time of the experiment.

The other instruments listed in Table 4 all performed as anticipated thus indicating their suitability for launch into space. However, the shortness of the mission obviously prevents any complete analysis of the suitability of these components for long-term space operation.

4.3 Measurements on Future Space Missions

4.3.1 Space Station Freedom

Upon its completion, (probably in the late 1990's) Space Station *Freedom* (SSF) will be the largest, most complex spacecraft in orbit. This, and the fact that SSF will be deployed in a low earth-orbit with a 30 year life expectancy, make the anticipated measurement requirements of SSF of significant interest to the SDI. The types of measurements, the details of the sensors, and the long-term performance of the devices will all be of consequence in the design of low-earth orbit SDI platforms. However, because of the complexity of the station and the present uncertainties of the design, it is somewhat difficult at this time to discuss the specific measurement requirements and techniques anticipated for SSF. This portion of the report will therefore consist primarily of a general discussion of the parameters that will have to be measured on the space station and their anticipated magnitude and required uncertainties. A somewhat more detailed discussion of the metrology requirements of SSF is presented in two recent reports prepared for NASA [25, 26].

As mentioned before, the measurement requirements of the space station will be extremely diverse because of the size and complexity of the spacecraft. Table 5 summarizes the main subsystems planned for SSF. Even though each of these subsystems will have some unique metrology requirements, the general measurement requirements exhibit many similarities. To provide an example of the types of housekeeping measurements that will be required for the operation of SSF, Tables 6, 7, and 8 summarize the metrology requirements of the Environmental Control and Life Support System, the Electrical Power System, and the Propulsion System, respectively. Obviously, the numbers presented in these tables are subject to change as the design plans for SSF are finalized. However, the general conclusions that can be drawn from

Table 5. Anticipated major subsystems of Space Station Freedom

Environmental Control and Life Support System (ECLSS)
Extra Vehicular Activity (EVA) System
Scientific Experiments
Electrical Power System (EPS)
Data Management System (DMS)
Mechanical Systems
Fluid Management Systems
Propulsion System
Servicing System
Guidance, Navigation and Control (GN&C) System
Communication and Tracking (C&T) System
Thermal Control System (TCS) and
Manned Systems (Hab and Lab Modules)

the information in Tables 6, 7, and 8 are unlikely to change significantly with subsequent design modifications.

As compared with the extreme magnitudes of many of the parameters anticipated for various SDI systems [1], the measured quantities and the required uncertainties listed in Tables 6, 7, and 8 are quite moderate, and as such the short-term measurement of these quantities is relatively routine. In many regards, the more extreme measurement and calibration requirements will be determined by the space-station user experiments. For example, the possible electrical measurement requirements shown in Table 9 for user experiments onboard the space station far exceed the requirements of the SSF power systems as listed in Table 7. Many of the measurement capabilities required by space-station users will be provided by the laboratory-support equipment (LSE) which is to be installed on the station. Table 10 shows a preliminary list of the devices planned for the LSE.

Because of the proposed 30-year lifetime of SSF, a primary design concern is the long-term operation and calibration of the measurement sensors and of the LSE. For many of the proposed sensors, the effects of long-term interaction with the low-earth orbit environment are presently unknown. So in a very real sense, the operational performance of the space station will represent a large body of data from which SDI designers can draw.

The question of calibration procedures on the space station is also of interest. Drifts in the sensors on SSF are unavoidable, so some method of re-calibration of these sensors is required. Three possible methods are 1) to replace the unit with a new sensor calibrated on earth, 2) to perform calibration of the unit on-orbit using reference standards which are periodically recalibrated on earth, or 3) to perform calibration of the unit on-orbit using self-sustaining (primary) on-orbit reference standards. Option (1) is the simplest possibility, but over long-term operation is the most expensive in

Table 6. Metrology requirements for environmental control and life support system of Space Station Freedom

Measurement Requirement	Range	Uncertainty	Anticipated Measurement Technique
CO_2 Content	3–12 mm Hg	1.0 mm Hg	CO_2 specific sensor
O_2 Content	115–205 mm Hg	5.0 mm Hg	Oxidizing/catalyzing electrochemical sensor or atomic absorption
Trace Contaminants	0.01–100 ppbv	10%	Gas chromatography and/or mass spectrometry
O_2/N_2 Supply Pressure	10–5000 psi	3%	Pressure transducer
Cabin Pressure	10–14.7 psi	0.1 psi average, 0.003 psi/minute	Pressure transducer
Fire/Smoke Detection	To be determined	To be determined	UV sensor, temperature sensor, or ionization chamber smoke detector
Cabin Temperature	60–90 °F	1 °F	Thermistors, Resistance Temperature Device (RTD)
Humidity	25–75% RH	5% RH	Semiconductor Sensor
Air Flow (ventilation)	5–200 ft/min (10–125 ft^3/min)	10%	Venturi flow meter
Water			
-pH	6–8 pH	0.2 pH	OH probe
-Ionic Species	0.01–50 mgm/l	1.0%	Specific ion probe
-Conductivity	10–100 μmho/μm	10%	Conductivity Probe
-Organics	0.1–1.0 mgm/l	10%	To be determined
-Particulate	0.2–2.0 mgm/l	10%	Optical detector
-Volume		5%	Level sensor or diaphragm

Table 7. Metrology requirements of the electrical power system of SSF.

Measurement Requirement	Range	Uncertainty	Anticipated Measurement Technique
Output voltage	0–440 V	0.5%	A-D converter
Output current	0–300 A	0.5%	Viewing resistor or current transformer
Solar radiation intensity	0–0.15 watts/cm^2	1.0%	Photometer
Solar Array pointing angle	±55 deg.	0.5 deg.	Sun sensor (photometer)
Photovoltaic temperature	−25 to 105 °C	0.2 °C	Platinum resistance thermometer
Solar dynamic temperature	0–750 °C	10°C	Platinum resistance thermometer
Battery charge	0–81 amp hrs	2.0%	Current and voltage sensors
Battery pressure	0–2000 psi	2.0%	Strain guage
Battery temperature	−100 to 200 °F	0.5%	Resistance temperature device
Insulation	10^3-$10^{10}\Omega$	10%	Megohm meter

Table 8. Metrology requirements of the propulsion system of SSF.

Measurement Requirement	Range	Uncertainty	Anticipated Measurement Technique
Thruster Force	0-100 lbs	1.0%	Load cell
Thruster Flow Rate	0–1 lb/hr	2.0%	Flow meter
Thruster Pressure	0–500 psi	2.0%	Pressure sensor
Thruster Temperature	Cryogenic to 2000 °F	20 °F	Platinum resistance thermometer or Type "S" thermocouple
Thruster Current	0–1 A	5.0%	Viewing resistor or current transformer
Propellant Pressure	0–3000 psi	2.0%	Pressure sensor or strain guage
Propellant Temperature	-200 to 400 °F	2.0%	Resistance temperature device

Table 9. Anticipated electrical requirements for space station user experiments.

Units	Range	Accuracy
DC Volt	1μV–20 kV	10 ppm
AC Volt	1 mV–20 kV	200 ppm
Ohm	1 $\mu\Omega$–100 $\mu\Omega$	0.01%
Impedance	1 $\mu\Omega$–100 $\mu\Omega$	1%
Frequency	10^{-9}–10^{10}	1 ppm

terms of the cost of transporting weight into orbit since every sensor must be sent back to earth for repair and recalibration. Option (2) is therefore preferable since only the primary standard will be returned to earth at periodic intervals. However, there are difficulties inherent in this method. Sending a ground-based reference standard into space, does not guarantee that its performance will be the same as on earth. The effects of the space environment, launch stresses, and micro-gravity must be taken into account when choosing the standard. Additionally, most ground-based standards are not designed with the size, weight, and power restrictions required by space use. It is also important to note that this second option requires the existence of a calibration laboratory and metrology-trained personnel aboard the space station. The last option (3) for providing calibration services for SSF is obviously the most favorable in terms of launch costs since no sensors or standards need to be transported to the station after

Table 10. Preliminary list of laboratory support equipment (LSE) on SSF.

Passive Dosimeter
Battery Charger
Life Sciences Glovebox
Equipment Washer/Sanitizer
Fluid Handling Tools/System
Microscope System
Refrigerator (4 °C)
Freezer (−20 °C)
Cameras
Camera Locker
Radiation Shielded Locker
Digital Recording Oscilloscope
Digital Multimeter
General Purpose Hand Tools
Cleaning Equipment
Freezer, Cryogenic (−196 °C)
Centrifuge, Refrigerated
Small Mass Measurement Device
Micro Mass Measurement Device
pH Meter/Ion Specific Analyzer
Spectrophotometer, UV/Vis/IR
Specimen Labeling Tools/Device
Freeze Drier
Digital Thermometer
Surgery/Dissecting Tools
Incubator
Freezer (−70 °C)
Laboratory Sciences Workbench
Ultrasonic Imaging System
Gas Chromatograph/Mass Spectrometer
High Performance Liquid Chromatograph

Table 11. Number of different measurements on the Hubble Space Telescope

Number of measurements	Type
2200	Digital Bi-levels (on/off)
730	Computer Software related (i.e. parity)
715	Temperature
500	Voltage and Resistance
351	Counters
280	Position
100	Current
100	Time Relationships
60	Power
60	Rates
20	Magnetic Fields
20	Strain
17	Velocity
6	Pressure

the initial fabrication of the on-orbit calibration facilities. However, the development of self-sustaining, on-board calibration capabilities will require a large research effort into the development of intrinsic (quantum mechanical) standards. Many of these are presently being developed and show great promise as new standards for several different parameters [1], but space deployment is a long way off. In the long-term, the utilization of the properties of the natural space environment (background fields, radiation levels, and various electromagnetic spectra) in the development of reference standards may enable the complete separation of space-based calibrations from earth-based standards. It is the progression by the space station toward option (3) that is of interest to SDI since the unmanned nature of the space platforms requires remote, autonomous calibration of sensors which in turn requires many of the same long-term space-based standards as on the space station.

4.3.2 Hubble Space Telescope

When launched in early 1990 the Hubble Space Telescope (HST) will be the most complex satellite in orbit.[2] Its high complexity and long anticipated mission life (15–30 years) make the performance of the HST of significant interest to SDIO. At most recent count, 5706 parameters are routinely measured and the values transmitted back to earth for status and control applications. All together, 20–25 different types of measurements are made (depending upon how one groups them). Table 11 summarizes the distribution of measurement types for the major categories.

[2]Since the original writing of this report, the Hubble Space Telescope has been launched. Reports on performance of the diagnostics will, however, not be available for some time.

From a metrology point of view, temperature measurements are of primary importance for the operation of the HST. Most of the temperature sensors are thermistors used to monitor the temperature of the mirror. Thermocouples will be used to monitor the heaters which maintain the mirror's constant temperature. Temperature magnitudes on the telescope will range from -100 °C to 60 °C with sensor uncertainties of about 0.1°C over a 5 °C range.

Voltage measurements will primarily monitor the 28 V dc power supplies and measurements will have approximately 0.1% uncertainty. Power measurements will be in the 10–100 watt range, pressures will be in the near-vacuum regime, magnetic field magnitudes are near one milligauss, and most of the strain measurements are to determine the effects of liftoff.

Because of the high complexity of the HST, a fair amount of effort has been put into investigating the possibility of controlling the housekeeping activities of the telescope using "expert systems." However, at this time it is still planned that the HST will be under primarily direct human control with the over 5000 diagnostics either providing information on demand or raising a "flag" if an inappropriate reading is recorded. This is obviously an inappropriate operation mode for SDI space hardware, but NASA's progress in automating the HST over the years will be of direct use in designing the operating systems for SDI platforms.

Another point of interest concerning the HST is the fact that NASA is building an "exact," operational duplicate of the HST at the Goddard Space Flight Center. The purpose of this simulator is to enable the diagnosis of malfunctions and to aid in the planning of repair procedures. Repairs would then be performed by space shuttle personnel and defective components would be returned to earth to be tested in the simulator to determine the cause of failure. It should be noted that certain components on the HST are anticipated to have a limited lifetime (for example, certain photomultiplier tubes are expected to last only 2.5 years). Thus scheduled maintenance visits by the space shuttle will be necessary to maintain the operation of the HST even if all components perform as anticipated. This highlights the extreme difficulties inherent in maintaining the long-term remote operation of a complex space facility, and indicates some of the many difficulties SDIO needs to overcome before deployment.

4.3.3 Galileo Space Probe

The Galileo space probe was launched in October 1989 with arrival at Jupiter in December of 1995. Galileo is the follow-up mission to the Voyager investigations of Jupiter and has the primary objective of investigating the Jovian atmosphere [27]. The spacecraft consists of two main pieces: the orbiter and the entry probe. The orbiter will perform remote sensing investigations from an orbit around Jupiter, while the entry probe will make the first direct measurements of the Jovian environment

Table 12. Galileo instruments with atmospheric objectives

Instrument	Location
Atmospheric structure instrument	Entry probe
Neutral mass spectrometer	Entry probe
Helium abundance interferometer	Entry probe
Nephelometer	Entry probe
Net flux radiometer	Entry probe
Lightning and radio emission detector	Entry probe
Solid state imaging system	Orbiter
Near infrared mapping spectrometer	Orbiter
Photopolarimeter–radiometer	Orbiter
Ultraviolet spectrometer	Orbiter
Radio science	Orbiter and Probe

while actually descending into the atmosphere. The sensors on the entry probe will be exposed to a harsher environment than any other space-based sensors to date.

Like the Voyager probes discussed earlier, the spacecraft subsystems were designed with high reliability components and extensive redundancy. Appropriate radiation hardening and shielding were used to increase Galileo's resistance to radiation effects although the actual radiation tolerance design requirements were less than those required for the Voyager spacecraft [28]. The housekeeping-type measurements will be primarily of parameters with very moderate magnitudes. Hundreds of temperatures are to be monitored in the −200 °C to 310 °C range using platinum wire transducers. Voltages up to 30 V dc are monitored using A-D converters, and currents from 0–15 amperes dc and 0–6 amperes ac will be measured. Also, piezo-electric crystal sensors will be used to measure the accumulation of surface contaminants on exterior surfaces, and the pressures in the propellant tanks will be monitored. All data from the engineering (housekeeping) subsystems will be 8-bit measurements, while scientific data will be 12–16 bit measurements.

While the performance of the engineering subsystems may be of limited use to the SDI programs, a study of the interaction of the scientific instruments and sensors aboard Galileo with the near-Jovian space environment will provide some important information for future SDI sensor development. Table 12 lists the instrument packages on the Galileo orbiter and entry probe. In the following paragraphs, the anticipated operation of the instruments of most interest to SDI are discussed. In-depth descriptions of these instrument packages may be found elsewhere [27].

The operation of the Atmospheric Structure Instrument (ASI) will be of particular interest to the designers of future space sensors for SDI applications. The ASI will measure temperature, pressure, density, acceleration, and altitude as the probe descends into the Jovian atmosphere. The actual operation of the devices will only be for approximately 60 minutes, but the sensors will have to survive 6 years of dormant

Table 13. Galileo Atmospheric Structure Instrument parameter summary

Typical altitude resolution	0.1 km
Altitude difference accuracy	~1%
Pressure accuracy	~1% of measured pressure
Pressure dynamic range	0.1 to 28 bars
Pressure resolution	0.1% of full scale on each range
Temperature range	0 to 500 K
Temperature accuracy	~1 K
Temperature resolution	0.12 K (12 bit A/D conversion)
Response times	0.3–16 ms
Vertical flow velocities, threshold	~1 ms^{-1}
Acceleration dynamic range	3×10^{-6} to 4×10^{-2} g_E
Acceleration accuracy	within ~100 ppm

storage during the trip to Jupiter. Also, the devices will be operated to destruction thus providing additional information about failure mechanisms.

The temperature sensor on the ASI is a dual platinum-resistance thermometer mounted on the exterior of the entry probe and has a high heat-transfer coefficient and low thermal inertia so it is well coupled to the atmosphere. Atmospheric temperatures are expected to vary between 100 and 450 K during the operation of the sensors. Pressures will be monitored between 100 mbar and 10–20 bar range by 3 pressure sensors outside of the probe boundary layer during descent. Pressure will be sensed by deflection of a stainless steel diaphragm which changes the reluctance in a magnetic circuit. Three pressure ranges will be monitored: 0.5, 4, and 28 bars. The acceleration of the probe (and subsequently the altitude) is determined by a 3-axis accelerometer mounted near the center of gravity of the probe. A summary of the ranges and uncertainties of the measurements made by the ASI is shown in Table 13.

The operation of the Neutral Mass Spectrometer (NMS) on the entry probe will be of interest to SDI because of the proposed use of mass spectrometers on SDI platforms to detect leaks, measure partial pressures, and determine the effects of effluents on the platform. The NMS on the Galileo probe is a 15 cm hyperbolic rod quadrupole with an electron impact ion source and a continuous channel secondary electron multiplier. The spectrometer has a mass range of 1 to 150 AMU with a dynamic range of 10^8. It will be used primarily to determine abundances and isotope ratios of major and minor atmospheric constituents.

The Helium Abundance Interferometer (HAD) is a device designed to measure the relative abundance of helium to hydrogen in the lower Jovian atmosphere. This ratio is determined by passing two parallel coherent beams of light through two identical gas chambers; one containing a Jovian atmosphere sample, the other a well characterized reference sample carried from earth. The interference patterns produced by combining the two beams of light determine the relative concentrations in the Jovian sample.

Besides the scientific data obtained by this experiment, the operation of this device will be of interest because of the information that will be supplied concerning the performance of the light sources (GaAs LED's) and optics (splitter, combiner, filters, etc.), and the ability of the system to maintain a well defined reference gas. It should also be noted that some very sensitive temperature and pressure sensors are included in this instrument in order to maintain identical temperatures and pressures in the two sample chambers.

The Photopolarimeter-Radiometer (PPR) is a device mounted on the Galileo orbiter which basically measures the temperatures and pressures of Jupiter's upper atmosphere using photometric, polarimeteric, and radiometric measurements. The determination of the temperatures of the many optical surfaces is very important and a multitude of thermistors are used to monitor these temperatures which average about $-5°C$. Long-term calibration of the detectors is also of importance and is provided by internal and external calibrator lamps and by external photometric and radiometric calibration targets.

Scientific devices on Galileo and other future space probes obviously will contain sensors which will be useful in other applications. It becomes clear that as spacecraft become more complex, an in-depth study of the overall performance of experimental apparatus (in addition to the scientific information obtained) is useful in the future design of space platforms and power systems.

4.3.4 Mariner Mark II Space Probes

The Mariner Mark II (MMII) spacecraft has been designed for future exploration of comets, asteroids, and the outer planets [29]. It was designed to be a modular spacecraft that can be easily reconfigured for different missions outside of the inner solar system. At present, two missions using the MMII are planned for the 1990's: the Comet Rendezvous Asteroid Flyby Mission (CRAF) in 1995 and the Cassini Mission to Saturn in 1996.

The MMII spacecraft subsystems are in many ways similar to those on the Voyager and Galileo spacecraft systems and thus require relatively routine system measurements for operation and control. The power system requires voltage measurements of magnitudes on the order of 30 V dc and current measurements of magnitudes less than 10 A. With the exception of the elevated temperatures on the RTG's and radiators, the critical temperatures on the spacecraft will range from -20 to $+40°C$ with temperature control being provided by a central heating system utilizing the excess heat from the RTG's. [30] Overall, the most stringent measurement requirements on the MMII probes will be involved with the scientific experiments and not with the operation of the actual spacecraft system. With this in mind, a brief review of the anticipated scientific hardware which is to be flown on the two planned MMII missions is presented below.

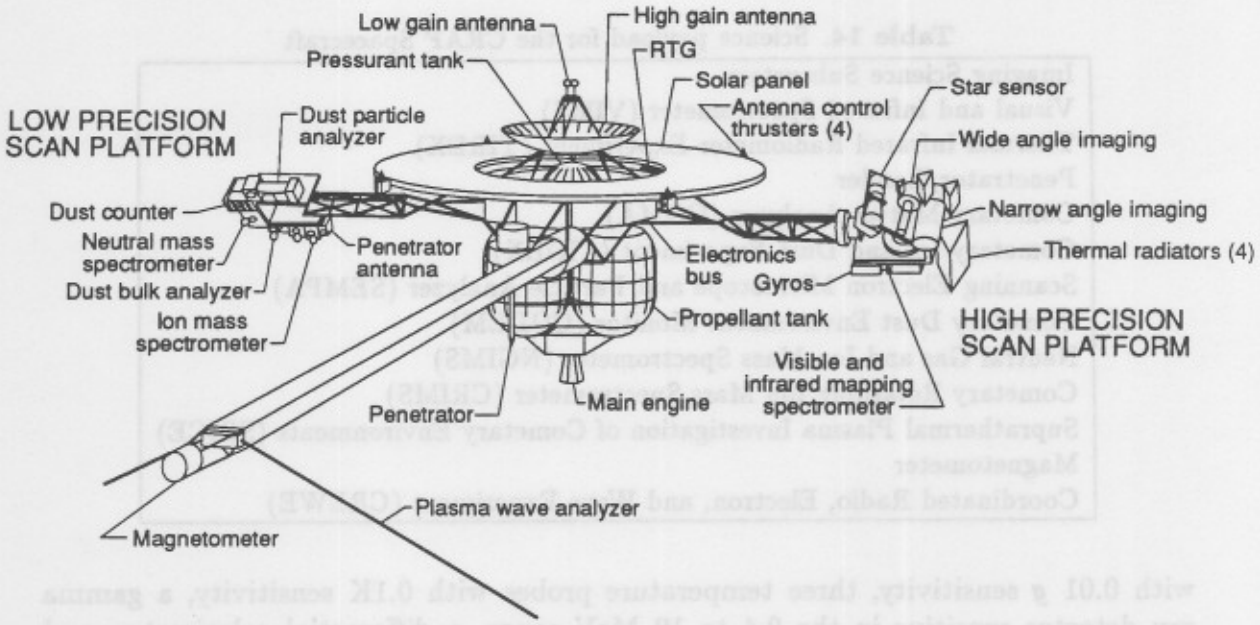

Figure 14. Schematic drawing of the comet rendezvous asteroid flyby spacecraft.

• Comet Rendezvous Asteroid Flyby (CRAF)

The CRAF mission is the first scheduled MMII mission and is presently planned to make a high spatial resolution survey of an asteroid, and then to rendezvous with a comet for long term investigations. [31] The total length of the mission is anticipated to be approximately 8 years with the comet rendezvous lasting about 3 years [32]. The CRAF spacecraft configuration is shown in Figure 14. As with the Voyager and Galileo missions, the spacecraft has been designed to protect against single point failures. The parts radiation requirements for CRAF will be much less than the design requirements of Voyager and Galileo, but CRAF must be designed to operate in the dusty environment around the comet.

CRAF will carry 13 scientific instruments which are listed in Table 14. A brief summary of the experiments whose operation will be of most interest to SDI is given here, while a more complete description may be found elsewhere [31], [22]. Many of these instruments are still in the design phase so details of control and operation are still somewhat sketchy. However, it is evident from the high complexity of these apparatus that a significant level of complexity for measurement and control will be required for their operation.

The first three experiments listed in Table 14 will basically map the comet nucleus, tail, and coma over a wide range of wavelengths to determine size, shape, chemical composition, and thermal properties. The Penetrator/Lander will acquire data about the evolution of the comet surface. The 1.5-m-long Penetrator/Lander will be propelled by a rocket motor into the nucleus and will contain six accelerometers

Table 14. Science payload for the CRAF Spacecraft

Imaging Science Subsystem
Visual and Infrared Spectrometer (VIMS)
Thermal Infrared Radiometer Experiment (TIREX)
Penetrator/Lander
Cometary Matter Analyzer (COMA)
Cometary Ice and Dust Experiment (CIDEX)
Scanning Electron Microscope and Particle Analyzer (SEMPA)
Cometary Dust Environment Monitor (CODEM)
Neutral Gas and Ion Mass Spectrometer (NGIMS)
Cometary Retarding Ion Mass Spectrometer (CRIMS)
Suprathermal Plasma Investigation of Cometary Environments (SPICE)
Magnetometer
Coordinated Radio, Electron, and Wave Experiment (CREWE)

with 0.01 g sensitivity, three temperature probes with 0.1K sensitivity, a gamma ray detector sensitive in the 0.4 to 10 MeV range, a differential calorimeter, and a gas chromatograph to analyze the gas produced by the calorimeter. The next 5 experiments (COMA, CIDEX, SEMPA, CODEM, NGIMS) will analyze the properties of the cometary dust and gas using secondary-ion mass spectrometry, X-ray fluorescence, gas chromotography, mass and velocity determinations, and quadrupole mass spectrometry. Each of these experiments is very complex when compared with apparatus flown on previous deep space missions. The last 4 experiments listed (CRIMS, SPICE, the magnetometer and CREWE) will analyze the processes which occur in the regions surrounding the comet. The CRIMS and SPICE experiments both contain mass spectrometers to measure ion temperature, mass, energy, and density along with electron energies. The magnetometer measures vector magnetic fields from 0.005–44,000 nT.

• The Cassini Project

The Cassini project is the second planned MMII mission. Its purpose is to provide an extensive orbital tour of the Saturn system (including flybys of each of Saturn's moons) and the sending of a probe to the moon Titan. As stated before, the basic spacecraft will be the same as for the CRAF mission. The scientific payload will obviously be different in detail, but will in many ways be similar in principle to the experiments onboard CRAF. Details of the Cassini experimental payload can be found in reference [29] and references therein.

Overall, it appears that there is little to be learned by SDI from the basic "housekeeping" operation of the Mariner Mark II spacecraft. The low power requirements, and minimal metrology needs make the MMII spacecraft operation orders of magnitude simpler than the requirements of SDI platforms. However, SDI could benefit from the experience which NASA accumulates from operating the extremely complex

scientific payloads aboard the MMII spacecraft for long periods of time (years) in fairly hostile environments (i.e. around a comet and near Saturn). As stated before, these experiments will represent some of the most complex and sensitive experimental devices sent into space. The long-term remote operation of these apparatus will be a significant challenge and will address many of the same operational problems facing the deployment of SDI platforms.

4.3.5 SPEAR II

The SPEAR II project is a continuation of the Space Power Experiments Aboard Rockets program which began with the SPEAR I launch (see section 4.2.4). The purpose of the SPEAR II experiment is to further investigate the use of natural space near-vacuum for high voltage insulation, and to determine the viability of using newly developed terrestrial pulse power technology in space. The payload will be launched by a sounding rocket in 1990 and the length of the experiment will be short (~222 s). In order to reduce outgassing from the payload surfaces and therefore eliminate the high background pressures which plagued SPEAR I, the payload bay will be pumped-down on the launch pad.

The SPEAR II payload consists of two experiments which are described in detail elsewhere [34]. Here we will briefly summarize the two experiments and concentrate on the sensors which will be used to monitor the payload. The first experiment is a high-voltage study which will be conducted up to 100 kV. All of the high-voltage components will utilize vacuum as an insulator rather than the solids and liquids normally used on earth. The load for the high-voltage experiment is the electron beam section of an RF tube which could later be used as part of a space-based free electron laser. The high-voltage circuitry will provide power-pulse bursts to the load of one second duration at a 50 Hz rate and the overall performance of the system will be monitored. The anticipated diagnostics are as follows: Klystrode heater voltage and the pulse-transformer primary and secondary currents will be measured using current-viewing resistors. The pulse-transformer primary and secondary voltages will be monitored with compensated resistance probes, and the output from the pulse-forming network will be determined using a current-sensing coil.

The second experiment will use a high-current (140 kA) load consisting of a plasma accelerator (or electromagnetic launcher). Two high-current discharges will be initiated during the course of the flight. The diagnostics which will be used to monitor the apparatus during these discharges are $\dot{B}$ probes to determine the plasma arc position, RC-compensated probes for the muzzle, breech, and inductor voltages, a current viewing resistor for the inductor current, and a differentiating Rogowski coil to monitor the switch current.

In addition to the sensors monitoring the high-voltage and high-current aspects of the experiment, a sophisticated external diagnostic package (EDP) will be used to

monitor the interactions between the spacecraft and the space environment. The instruments in the EDP are listed in Table 15 along with a brief summary [34] of each sensor.

Most of the sensors flown on SPEAR II are the same type of components used to make ground-based measurements. It will be of particular interest to see how these high-voltage and high-current sensors perform in the space environment. These first attempts at high-power measurements in space will provide the basis for the future design of high-voltage and current sensors for use on space nuclear power devices and SDI platforms.

4.4 Testing and Reliability of Space Systems

4.4.1 Introduction

As discussed in the two preceding sections, the base of knowledge concerning the reliability and causes of failure of existing spacecraft is an invaluable asset to the SDI program as it attempts to design long-life space platforms. Several studies [35], [36] have been performed which review the reliability and failure modes of many of the spacecraft launched between 1960 and the early 1980's, while Goddard Space Flight Center maintains a continuous published record of the reliability performance of its active satellites [37]. (It should be noted that in this section "reliability" refers to the ability of the spacecraft to perform its design function.) One of the conclusions from these studies is that the overall failure ratio (failures per operational year) has about doubled for spacecraft launched since 1977 versus those launched previously [38]. This is apparently not due to a decrease in the quality of parts or design, but to the increase in complexity of spacecraft built over the last three decades. A more meaningful measure of the relative reliability of recent spacecraft is shown in Table 16. This Table shows that recent satellites (post-1977) are generally more reliable since a much smaller percentage exhibit critical or single-point failures, and a much higher percentage experience only temporary failures. Data from Goddard Space Flight Center also indicates that recent satellites are more reliable and have longer lifetimes than earlier spacecraft (see Figure 15).

The fact that present-day spacecraft are generally more reliable than earlier spacecraft is encouraging for SDI applications. However, the fact that the overall failure ratio is increasing for newer satellites (primarily indicating an increase in temporary failures) must be addressed since SDI spacecraft must operate when required. In most cases temporary failures (or anomalies) cannot be tolerated. Additionally, it is interesting to note that Goddard spacecraft launched as late as 1983 have only about a 60% probability of achieving a useful lifetime of 5 years (see Figure 15). Thus it is evident that at this time the construction of a spacecraft with a lifetime of 10 years (as

Table 15. SPEAR II external diagnostics package (EDP) instrument complement

Instrument	Qty	Loc	Summary
Low Light TV Camera	2	E	White light detection of electrical breakdown, 8 images total; optical heads located in power section.
35 mm Film Camera	2	E	White light detection of electrical breakdown: 8 images total; optical heads located in power section.
Photometer	1	S	High time resolution detection of HV breakdown; 391.4 nm; photon-counting; photon mapping.
EMP D-dot Sensor	1	S	Measure EMP due to HV and HC experiments; 3-axis; 200 ns time resolution.
EMP B-dot Sensor	1	S	Measure EMP due to HV and HC experiments; 3-axis.
Charged Particle Detectors	2	S	1 eV to 20 keV ions and electrons, electrostatic analyzers
Thermal Plasma Probe (Langmuir Probe)	1	S	Ion and electron density; electron temperature at ionospheric range (n: 10^4 – 10^7, T: 500 K–5,000K.
Charge Probe	1	S	Vehicle potential changes.
Neutral Pressure	1	P	Capacitance manometer and cold-cathode ionization gauge; Range: 10 to 10^{-7} torr; high time resolution.
Magnetometer	1	S	3-axis fluxgate; ambient geomagnetic field measurements.
E=EDP Electronics Section; S=EDP Sensor Section; P=Payload Section			

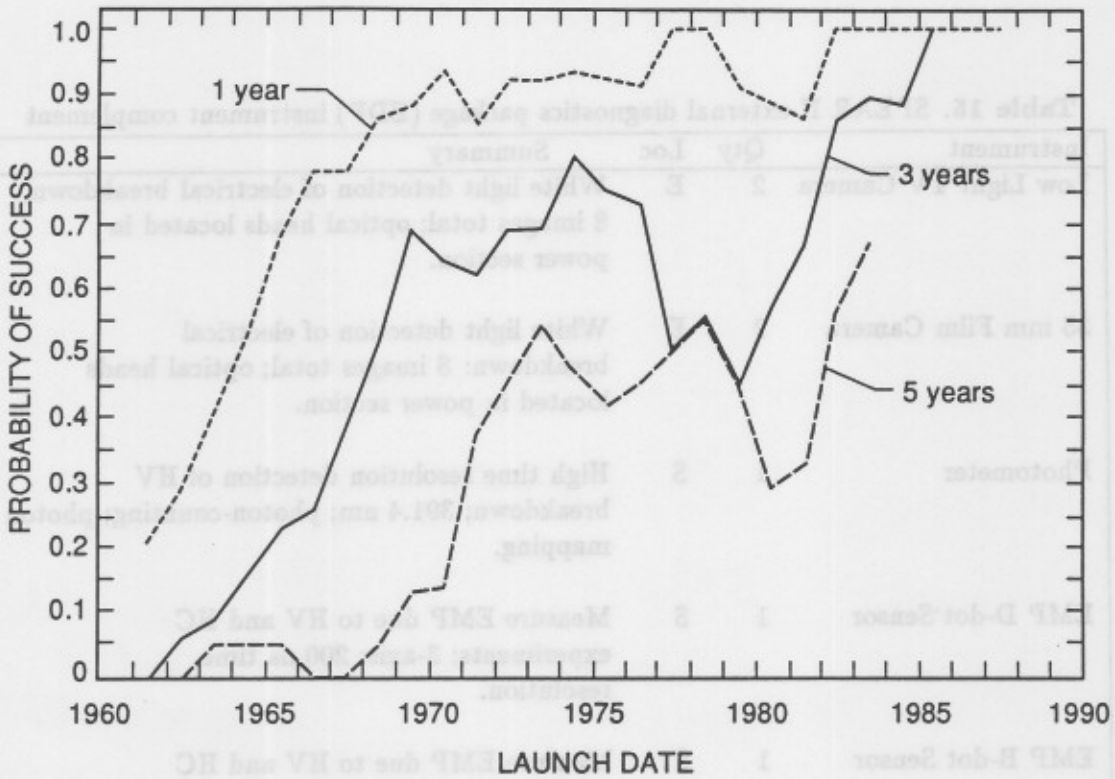

Figure 15. Probability of survival of Goddard satellites as a function of launch date

Table 16. Severity of failure for early and late programs

	Early programs		Late programs	
Description	Count	Percent	Count	Percent
Critical failure	186	10	18	3
Single point failure	160	8	28	5
Redundant unit	353	18	68	12
Work-around required	339	18	101	17
Degraded performance	499	26	117	20
Temporary failure	334	17	225	38
Others	52	3	32	5

required for SDI applications) is non-trivial even if the spacecraft is significantly less complex than required by SDI missions.

Further analysis of the causes of spacecraft failure indicate that design failures and unanticipated interactions with the space environment are the primary cause of recent spacecraft failures [38]. The increase in design failure is largely due to the increased complexity of recent spacecraft, and the difficulties with environmental interactions are a direct result of longer mission lifetimes. In the next two subsections of this report we will investigate some of the research and procedures currently taking place to reduce these types of failures.

Further investigation of spacecraft failures indicates that failure in recent space missions primarily occur in the telemetry, command, and control subsystem, or in the data management subsystem, or in the navigation subsystem. These subsystems are all presently being developed at an extremely rapid rate with new developments constantly being integrated into spacecraft. Thus the large failure rates are due to increasing complexity and the use of new technologies. These three subsystems must all be substantially developed before they will be able to meet anticipated SDI requirements.

It is interesting to note that a primary cause of failure of the spacecraft power systems is "unknown" [24]. This implies that the presently used space power systems are insufficiently instrumented (or monitored) and thus a cause of failure could not be determined. It is hypothesized that the failures in many of the new power systems may be related to the power conversion electronics, an area which is changing rapidly.

4.4.2 System Testing

Because of their expense and inaccessibility for repair, spacecraft represent some of the most highly tested hardware produced at this time. Everything from individual components to complete subsystems and launch packages are subjected to a large number of tests to determine resistance to launch, re-entry, and space environments. In this section we briefly discuss some of the pre-launch testing procedures used for spacecraft designed at Goddard Space Flight Center [39]. These tests give some indication of the range of conditions that present spacecraft are expected to survive.

Structural and mechanical tests are used to simulate the forces of launch and re-entry. These tests consist primarily of static stress, mechanical shock and vibroacoustic susceptibility. The magnitude of these tests are determined on a payload-by-payload basis although vibroacoustic tests are performed over a range of 20–2000 Hz. Pressure tests are also performed to ensure that the evacuation of the payload during launch does not cause sufficient pressure differences within the payload to cause structural deformation.

Electromagnetic (EM) compatability measurements are presently performed to ensure

that the EM emissions from other spacecraft do not interfere with the operation of the payload. Testing is performed at the component, subsystem, and payload levels. Each system must survive prolonged exposure to 2 V/m electric field in the frequency range of 14 kHz to 2 GHz, and 20 V/m fields from 2 GHz to 18 GHz. Magnetic fields applied to the spacecraft range from 30 Hz to 50 kHz with magnitudes approaching 50×10^{-4} tesla.

Vacuum, thermal, and humidity testing is performed on spacecraft in order to approximate some of the environmental stresses to which the payload will be exposed. Vacuum cycling down to $< 1 \times 10^{-5}$ torr is performed several times in order to determine the effects of vacuum and decompression on the hardware. Temperature cycling is also performed with the minimum and maximum temperature determined by the requirements of the individual spacecraft. The spacecraft can also be exposed to varying degrees of humidity (up to 95% relative humidity) to determine the effects of possible condensations during launch.

While present pre-launch testing requirements are fairly stringent, it is obvious that current procedures do not test several parameters which would be anticipated to affect SDI platforms. These parameters include radiation, hostile-threat interactions, and interactions with the space environment. How these conditions affect designs of various components, subsystems, and payloads will need to be addressed before deployment of long-term SDI space platforms is feasible.

4.4.3 Space Environment Effects

As mentioned in the previous section, little testing of the interaction of the space environment with a payload is performed prior to launch. This is primarily due to the difficulties in accurately simulating the space environment for long periods of time in a vessel large enough to house the spacecraft which is to be tested. This information must be obtained via small earth-bound experiments which attempt to simulate various aspects of the space environment to determine the effect on materials of long-term exposure, or by space-based experiments where materials and components are exposed to the low-earth space environment and then returned for study. Both types of experiments have their advantages. The earth-based experiments are comparatively inexpensive, and reasonably fast but often fail to reproduce the effects of real space exposure. The space-based experiments, on the other hand, are very expensive and are inaccessible for long periods of time. In this final subsection of this report, we review some of the ongoing experiments dealing with interactions of materials with the space environment and their implications for the reliability of anticipated SDI platforms.

Early shuttle flights have demonstrated that various polymers, carbon coatings, paints, and optical surfaces suffer changes in mass and optical characteristics when exposed to low-earth orbit [40]. Neutral atomic oxygen, which is extremely corrosive is the

major constituent of the low-earth orbit environment [41] and is hypothesized to be the cause of these observed degradations of materials. The corrosive nature of the atomic oxygen in low earth orbit (LEO) is sufficient to pose a threat to the long-term durability of solar arrays, mirrors, and other material surfaces being considered for use on SDI space platforms.

A significant amount of ground-based research is currently being performed to determine the effects of atomic oxygen interaction with various materials [42]. Initial results indicate that a large number of materials presently designated for space applications are adversely affected by exposure to atomic oxygen. For example, studies [43] have shown that the epoxy resin in fiberglass-epoxy composite materials used to support solar panels is removed by prolonged exposure to atomic oxygen. This allows the fiberglass fibers to be exposed and to possibly contaminate other systems. The development of coatings to protect various composites [43] and mirror surfaces [44] is proving to be promising. However, the use of protective coatings may be somewhat limited due to the susceptibility of the coatings to damage by impacts from microscopic debris [45]. The impact of a high-energy particle penetrates the coating and allows the atomic oxygen to erode the surfaces beneath the coating. Over time, this process could degrade the performance of mirrors and other optical surfaces. The severity of this degradation is difficult to predict at this time due to the differences between the simulated space environment and the real conditions present in LEO. Further experimentation must be done in order to determine the importance of this effect because of the reliance of several SDI projects on high-power and high-resolution optical systems.

To date, little data is available concerning the interaction of operating spacecraft and the LEO environment due to the difficulties in returning spacecraft to earth without the spacecraft interacting with the atmosphere upon reentry. In 1985, NASA launched the Long Duration Exposure Facility (LDEF) in order to obtain the information needed to plan the construction of LEO platforms such as the space station. The LDEF is a satellite which carried a vast array of experiments to determine the interaction of materials and components with the space environment. Items on the LDEF included polymers, plastics, composites, metals, glass, crystals, lubricants, electronic components (some active), power supplies, and optical components. Over one thousand material samples are on board the LDEF and the determination of surviving materials will be of extreme importance to SDI platform design. LDEF was only recently retrieved (late 1989) after 4 years of exposure, and results are yet to be disseminated.

Many future experiments dealing with interaction of the LEO environment with spacecraft are planned for deployment on the space station [46]. These experiments will include studies of the interaction of the space station with the space plasma, interactions with the earth's magnetic field, interactions with the solar wind, surface charging, ram and wake effects and collision induced ionization. While the activation

of these experiments is still a significant time away, they are presently in the planning stages and obviously SDI will benefit from the accumulated data.

4.5 Survey Conclusions

The conclusions which can be drawn from the survey of the space-based measurements are fairly general, and in many ways agree with the conclusions of our previous report [1]. All available information concerning the behavior and operation of existing systems in space is of importance to the SDI program. There exists a vast amount of data concerning the performance of various devices in space applications and it would be foolish to ignore these data when designing SDI-related hardware and experiments. Even more directly applicable information will be available in the future as more complex space systems (such as the space station and Hubble Space Telescope) are deployed and operated.

However, in a very real sense, the applicability of much of the available information concerning the reliability of space-based systems (measurement-related and otherwise) to the SDI program is severely limited. All the data on presently operating systems suffer from one or more shortcomings for SDI applications in that all present space systems are designed for short-term missions, or are comparatively low in complexity, or operate at very low power levels. Practically no space-based housekeeping measurements are presently being made which can be directly compared to those that will be required for SDI weapon platforms. This is an area of research which must be actively pursued in order that the measurement capabilities exist when they are needed.

It is also important to note again that few presently operating NASA spacecraft have operational lifetimes exceeding 5 years. This is only half of the anticipated lifetime of SDI platforms and present spacecraft are substantially less complex than those envisioned for SDI applications. Significant advances in the long-term survivability of spacecraft must be made before SDI will be viable.

A final point of importance is the fact that as the complexity of present spacecraft increases, the number of anomalies also tends to increase. While these anomalies tend to be only temporary failures, the rectification of the errors usually require interaction with ground-based systems (usually including human input). This solution is obviously unacceptable for SDI systems which must be able to operate reliably and autonomously when required. Thus the development of on-board software capable of responding to anomalies is essential to the reliable operation of SDI space systems.

5 SUMMARY

This report presents the results of three investigations to identify the present and anticipated metrology requirements of the SDI Space Power Program and on improving the measurement reliability of current and voltage sensors in both ground-based developmental systems and remote applications in space. The initial work provided a metrology assessment of the future SDI needs and the state of the art in measurement technology. The report identified areas where improvements in measurement accuracy are needed [1]. In this report, the metrology assessment has been followed up with an investigation into diagnostics that have already been flown on board spacecraft. In the area of measurement reliability, a technique has been developed and demonstrated capable of detection of 1% measurement nonlinearities in an electro-optic voltage measurement system. The error signatures for these voltage measurement systems have been characterized. Another task reported here is a study of the applicability of magneto-optic sensors to impulse current measurements. The optical fiber sensors studied in this work are capable of measuring submicrosecond-risetime current pulses in the 100 ampere range. However, improvements are required for better stability and thereby better accuracy. Noise in the measurements is also significant, and improvements in the light source and detectors are required to increase the measurement accuracy for low-amplitude current pulses.

Future work will include identification of measurement nonlinearities through comparison measurements with conventional sensors, i.e., through measurements with dual sensors in parallel. The implementation of improvements will continue in the magneto-optic current sensor to enable greater measurement accuracy. The aim of this work with both current and voltage sensors is to examine the feasibility and ultimately, to develop techniques to permit error detection, identification, and correction in remote measurement applications.

6 ACKNOWLEDGEMENTS

The authors wish to acknowledge the contribution of Dr. Gordon Day of the Electromagnetic Technology Division of NIST, who provided an annealed fiber current sensor for these studies. We would also like to thank Regina Von Feldt for her excellent typing of this manuscript. Our thanks are also due to Dr. Robert Kraus of W. J. Schafer Associates for providing valuable assistance and guidance.

7. REFERENCES

[1] Olthoff, J. K. and Hebner, R. E., *Assessment of Space Power Related Measurement Requirements of the Strategic Defense Initiative*, National Institute of Standards and Technology, Technical Note 1259, 1989.

[2] D. Graupe, *Identification of Systems*, Krieger, Malabar, Florida (1976).

[3] M. M. Adibi and D. K. Thorne, "Remote Measurement Calibration," IEEE Tr. Power Systems, Vol. PWRS-1, No. 2, May 1986.

[4] W. J. Kolarik, Editor, "Life Cyle Life Testing: Reliability Confidence Intervals," Technical Report TTU-TR-88-1, Texas Tech University (1988).

[5] W. J. Kolarik, Editor, "Dormant Phase Pulsed Power Availability Study," Technical Report TTU-TR-87-2, Texas Tech University (1987).

[6] R. J. Van Brunt, Ed., "Research for Electric Energy Systems – Annual Report," National Institute of Standards and Technology Report, NISTIR 4339, pp. 59–75, (1990).

[7] R. Boisvert, S. Howe, and D. Kahaner, *GAMS: Guide to Available Mathematical Software*, NBSIR84–2824, (1984).

[8] A. S. Gilmour, Jr., A. K. Hyder, Jr., M. F. Rose, *Space Power Technology*, SUNY at Buffalo, Buffalo, NY 14260 (1986).

[9] A. D. Kersey, M. A. Davis, "All-fiber Faraday-rotation current sensor with remote laser-FM based heterodyne detection," H. J. Arditty, J. P. Dakin, R. Th. Kersten, eds. Proceeding of the 6th International Conference, OFS '89; 1989 September 18–20; Paris, France. Berlin: Springer-Verlag; 1989 pp. 285–290.

[10] L. Li, J. R. Qian, and D. N. Payne, "Miniature optical fiber current sensors," Int. J. Optical Sensors, vol. 2, pp. 25–33 (1987)

[11] B.T. Neyer, J. Chang, and L.E. Ruggles, "Calibrated Faraday current and magnetic field sensor," SPIE vol. 566 Fiber Optic and Laser Sensors III, pp. 201–205 (205)

[12] R.E. Hebner, Jr. and M. Misakian, "Calibration of high-voltage pulse measurement systems based on the Kerr effect," National Bureau of Standards, NBSIR 77-1317 (Sept. 1977)

[13] T. W. Cease, "Field testing of a magneto-optic current transducer," Workshop on the Role of Optical Sensors in Power System Voltage and Current Measurements, National Bureau of Standards, Gaithersburg, MD, 1987.

[14] H.S. Lassing, A.A.M. Oomens, R. Woltjer, P.C.T. van der Laan, and G.G. Wolzak, "Development of a magneto-optic current sensor for high, pulsed currents," Rev. Sci. Instrum., vol. 57, no. 5, pp. 851–854, May, 1986

[15] A. J. Rogers, "A vibration-insensitive optical-fibre current sensor," SPIE vol. 630, Fibre Optics '86 (Sira), pp. 180–186 (1986).

[16] G. Day, A. H. Rose, "Faraday effect sensors: the state of the art," Proc. SPIE vol. 985, pp. 138–150 (1988).

[17] G. W. Day, P. D. Hale, M. Deeter, T. E. Milner, D. Conrad, S. M. Etzel, "Limits to the precision of electro-optic and magneto-optic sensors," NBS Technical Note 1307 March, 1987 (1987).

[18] R. Ulrich, S. C. Rashleigh, and W. Eickhoff, "Bending-induced birefringence in single mode fibers," Opt. Lett., vol. 5, 273–275 (1980).

[19] Kohlase, C. E. and Penzo, P. A., "Voyager Mission Description," Space Science Reviews, vol. 21, pp. 77–101, 1977.

[20] Space Science Reviews, vol. 21, 1977.

[21] Space Science Reviews, vol. 22, 1977.

[22] Laung, P., Whittlesey, A. C., Garrett, H. B., and Robinson, P. A., "Environment-Induced Electrostatic Discharges as the Cause of Voyager I Power-On Resets", J. Spacecraft, vol. 23, pp. 323–330, 1986.

[23] *"Functional Requirement Mariner Jupiter/Saturn 1977 Environmental Design Requirements,"* JPL-MJS77-3-240A, Jet Propulsion Laboratory, 1976.

[24] *SPEAR-1*, Final Report, Utah State University, 1988.

[25] Cotty, G. M., Ranganathan, B. N., and Sorrell, A. L., *On-orbit Metrology and Calibration Requirements For Space Station Activities Definition Study*, Final Report, Martin Marietta Manned Space Systems, 1989.

[26] Minskey, R. E., *Definition/Planning On-Orbit Metrology and Calibration Requirements for the Space Station "Freedom,"* Technical Report, Vitro Corp., 1989.

[27] Hunter, D. M., Cohen, L., and Hansen, J. F., "Atmospheric Science on the Galileo Mission," Space Science Reviews, vol. 44, pp. 191–240, 1986.

[28] *Functional Requirement Galileo Orbiter Environmental Design Requirements*, JPL GLL-3-240, Jet Propulsion Laboratory, 1989.

[29] Draper, R. F., "The Mariner Mark II Program," Meeting of American Institute of Aeronautic and Astronautics, Reno, NV, Jan., 1988.

[30] *Comet Rendezvous Asteroid Flyby (CRAF): Spacecraft Description*, JPL PD 699–008, Rev. F, Jet Propulsion Laboratory, 1987.

[31] *The Comet Rendezvous Asteroid Flyby Mission, A Search for our Beginnings*, JPL 400–320, Jet Propulsion Laboratory, 1987.

[32] *Outward to the Beginning*, JPL 400-341, Jet Propulsion Laboratory, 1989.

[33] Draper, R. F., *The Comet Rendzvous Asteroid Flyby Project,* Meeting of the 38th Congress of International Astronautical Federation, Brighton, OK, Oct., 1987.

[34] *SPEAR II*, Internal Report, W. J. Schafer Inc., 1988.

[35] Hecht, H. and Hecht, M., *Reliability Prediction for Spacecraft*, RADC Report RADC-TR-85-229, 1985.

[36] Bloomquist, C. and Graham, W., *Analysis of Spacecraft, On-Orbit, Anomalies, and Lifetimes,* Report No. PRC-R-3579, for NASA, Goddard Space Flight Center, 1983.

[37] Elsen, W. G., *Orbital Anomalies in Goddard Spacecraft for CY 1987,* Goddard Space Flight Center, 1988 and references therein.

[38] Hecht, M. and Fiorentino, E., *Causes and Effects of Spacecraft Failures,* Quality and Reliability Engineering Int., vol. 4, pp. 11–19, 1988.

[39] *General Environmental Verification Specifications,* Goddard Space Flight Center.

[40] Leger, L.L., *Oxygen Atom Reaction with Shuttle Materials at Orbital Altitudes,* NASA TM-58246, 1982.

[41] *U. S. Standard Atmosphere, 1976,* U. S. Government Printing Office, Washington, D. C., 1976, p. 30.

[42] Banks, B. A. and Rutledge, S. K., *Low Earth Orbital Atomic Oxygen Simulation for Materials Durability Evaluation,* 4th Int. Symp. on Spacecraft in Space Environment, Tolouse, France, September, 1988 and references therein.

[43] Rutledge, S. K., Paulsen, P. E., and Brady, J. A., *Evaluation of Atomic Oxygen Resistant Protective Coatings for Fiberglass-Epoxy Composites in LEO,* NASA TM 101955, 1989.

[44] Gulino, D. A., Egger, R. A., and Bamholyer, W. F., *Oxidation-Resistant Reflective Surfaces for Solar Dynamic Power Generation in Near Earth Orbit,* NASA TM 88865, 1986.

[45] Gulino, D. A., *Effect of Hard Particle Impacts on the Atomic Oxygen Survivability of Reflector Surfaces with Transparent Protective Overcoats,* NASA TM 88874, 1987.

[46] Garrett, H. B. and Evans, R. W., *Space Station Environmental Interactions Experiments Database,* Jet Propulsion Laboratory, Draft, 1986.